

Acoustical Measurement of Current and Vorticity beneath Ice

DIMITRIS MENEMENLIS

Electrical and Computer Engineering, University of Victoria, Victoria, British Columbia, Canada

DAVID M. FARMER

Ocean Physics, Institute of Ocean Sciences, Sidney, British Columbia, Canada

(Manuscript received 28 October 1991, in final form 1 May 1992)

ABSTRACT

An acoustical instrument has been developed to measure path-averaged horizontal current and vorticity in the subice boundary layer of the eastern Arctic during the spring of 1989. A triangular acoustic array of side 200 m was used to obtain reciprocal transmission measurements at 132 kHz, at 8, 10, and 20 m beneath an ice floe. Pseudorandom coding and real-time signal processing provided precise acoustic travel time and amplitude for each reciprocal path.

Mean current along each acoustic path is proportional to travel-time difference between reciprocal transmissions. Horizontal velocity normal to the acoustic paths is measured using scintillation drift. The instrument measures horizontal circulation and average vorticity relative to the ice, at length scales characteristic of high-frequency internal waves in the region. The rms noise level of the measurements is less than 0.1 mm s^{-1} for velocity measurements and $0.01 f$ for vorticity, averaged over 1 min. Except near the mechanical resonance frequency of the moorings, the measurement accuracy is limited by multipath interference.

Path-averaged horizontal velocity is compared to point measurements, and marked differences are observed due to local anomalies of the flow field. The integral measurement of current is particularly sensitive to the passage of internal waves that have wavelengths longer than the horizontal separation of the transducers. A comparison of horizontal velocity at two depths in the boundary layer shows good coherence at internal-wave frequencies, and some attenuation as the ice is approached. Relative vorticity at internal-wave length scales is dominated by horizontal shear caused by flow interaction with ice topography, and not by planetary vorticity.

1. Introduction

The concept of reciprocal acoustical travel-time measurements as a means of determining path-averaged currents is well established (Worcester 1977). Here we describe an instrument designed to exploit this principle in studies of the boundary layer just beneath the Arctic ice cover. Such measurements are of interest both because of the opportunity provided for comparison with the more commonly acquired point measurements and because of a particular configuration allowing determination of average vorticity, which cannot be achieved with the traditional approach; in addition, their unprecedented sensitivity allows detection of phenomena not observable with traditional sensors.

The current-measuring technologies typically used beneath sea ice are described by Morison (1989) and McPhee (1989). Moored and profiling mechanical current meters have been successfully used to measure turbulence and internal waves. Electromagnetic current meters, diode-laser Doppler velocimeters, and more

recently, acoustic Doppler current profilers have also been used. A common feature of all these measuring technologies is that they are inherently local in character. Because of irregularities in the underside of the ice, point measurements in the boundary layer are subject to local anomalies and fine structure and may not be representative of the mean flow field. Integral measurements of current provide a means of checking the validity of local observations.

Small-scale acoustical current meters, based on reciprocal travel-time measurements over a few centimeters, have been used to estimate the water drag coefficient of first-year ice (Shirasawa 1986). Worcester et al. (1985) extended the technique to the direct measurement of mesoscale ocean currents by using transceiver separations of several hundred kilometers. At those length scales, the problem is complicated by the existence of multiple acoustic paths and the effects of sound-speed structure. Our measurements are made in the well-mixed layer adjacent to the floe, where the effects of sound-speed variability are negligible. The horizontal separation of the transducers is 200 m, and the pulse length allows resolution between the direct and ice-reflected paths for measurements made within a few meters of the lower surface of the ice. The shorter

Corresponding author address: Dr. David M. Farmer, Institute of Ocean Sciences, P.O. Box 6000, Sidney, B.C. Canada V8L 4B2.

range, however, requires travel-time measurements that are a few orders of magnitude more precise than those described by Worcester et al. Because of its dimensions, the acoustic current meter is particularly sensitive to the passage of high-frequency internal waves under the ice camp.

Horizontal velocity normal to the acoustic paths can be determined by measuring scintillation drift. Sound traveling through a medium having random fluctuations in refractive index suffers perturbations that cause amplitude and phase scintillations on a receiving plane. These scintillations can be used to study the sound-speed fine structure and large-scale motions of the intervening fluid (Farmer et al. 1987). The acoustic array in the Arctic is used to investigate the applicability of the scintillation technique to the study of the ice-water boundary layer.

Müller et al. (1986) pointed out the importance of the potential vorticity mode of motion that must coexist with internal gravity waves at small scales. Because relative vorticity and horizontal divergence are difficult to measure, the vortical mode of motion has traditionally been ignored. Müller et al. (1988) used a triangular current-meter array to estimate potential vorticity at small scales in the ocean. They calculated relative vorticity and horizontal divergence, not from a continuous line integral, but from measurements at three discrete locations. This causes significant sampling errors. Rossby (1975) suggested a better method for measuring relative vorticity. He pointed out that the difference in travel times of acoustic signals traveling in opposite directions around a closed ring of transceivers provides a direct measurement of the enclosed average relative vorticity. Longuet-Higgins (1982) showed that a ring of four instruments will determine the scalar vorticity and its horizontal gradient, while a ring of five instruments can also determine the Laplacian of the vorticity field. Winters and Rouseff (1990) proposed a filtered

backprojection method for the tomographic reconstruction of vorticity in a moving fluid with variable index of refraction. Ko et al. (1989) demonstrated the feasibility of measuring mesoscale ocean vorticity from acoustic measurements. This paper reports the use of this technique to measure vorticity at internal-gravity-wave length scales in the boundary layer just a few meters beneath the Arctic ice cover.

2. Instrumentation

The acoustic system consists of six underwater units grouped in three clusters located at the corners of a horizontal triangle of side 200 m (Fig. 1). At each corner, sonars are deployed at two separate depths beneath the ice. The depth of each triangular array may be manually adjusted between 8 and 20 m. The underwater units are connected to surface electronics contained in a centrally located instrument hut through multiconductor cables. At regular intervals, each sonar emits a coded acoustic signal that is received, digitized, and decoded in real time by the other units. The accompanying electronics allow precise measurement and recording of acoustic amplitude and travel time. The simultaneous reciprocal travel-time measurement at frequent intervals along each side of the triangular array provides the basic dataset from which velocity and average vorticity are subsequently determined.

The quantity of digital information generated by the system poses a formidable processing and storage challenge. The raw data consists of 24 16-bit channels sampled at 44 kHz. In order to reduce the required recording bandwidth, decoding of the acoustic signal and data reduction are carried out in real time by each sonar. Serial data streams from the sonars are then dispatched to the surface where they are interleaved and stored on videocassette-recorder tapes using digital audio technology.

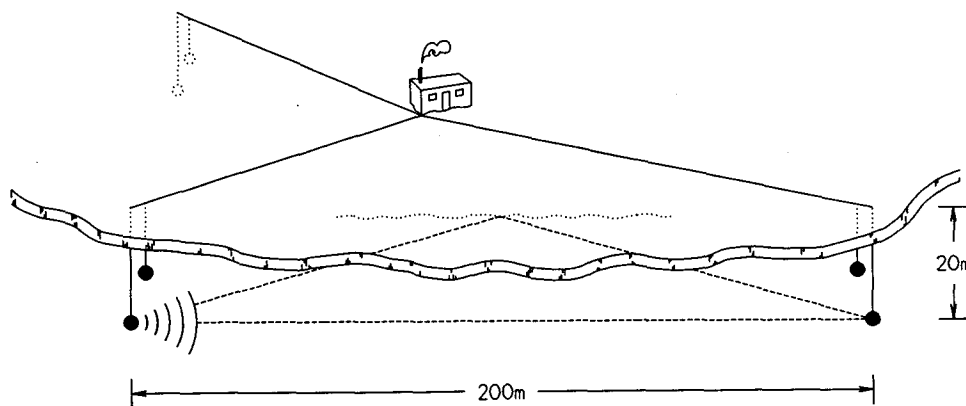


FIG. 1. Schematic representation of the acoustical system. Underwater units were deployed at two depths at the corners of a horizontal triangle. Velocity and average vorticity are obtained from reciprocal travel-time measurements along each side of the array. The direct and ice-reflected acoustic ray paths are depicted for a pair of transmit-receive sonars.

a. Deployment

Each underwater unit consists of two sonars mounted on a steel bar and suspended from the ice (Fig. 2). The use of paired sensors was intended both to explore the possibility of scintillation analysis and also to provide redundancy. Adjustment of sonar depths was achieved by energizing 1-kW heating wires embedded in slotted PVC (polyvinyl chloride) tubes surrounding the cables where they passed through the ice. The heating wires melted the water inside the tubes, thus freeing the cables for depth adjustment.

b. Surface electronics

The surface modules are responsible for the generation of the analog transmission signal, the timing and control of the acoustic system, and the storage and monitoring of the digital data collected by the sonars (Fig. 3). The timing and control unit supplies all system clocks. It derives the clock reference from a pulse-code-modulation encoder, divides it as required, and distributes it to the transmit-signal generator and the sonars. This unit also controls transmit timing and sequencing. The transmit-signal generator produces the pseudorandom code for transmission. The junction box acts as a traffic controller for signals between the sonars and the rest of the instrumentation; on one side it receives wiring from the surface electronics, while on the other there are connectors that constitute the starting point of the underwater cables. The data-recording unit receives processed digital data from the underwater units and stores the data on video tapes using a pulse-code-modulation encoder. A personal computer is used to specify the transmission sequence, control the sonars, and validate the collected data.

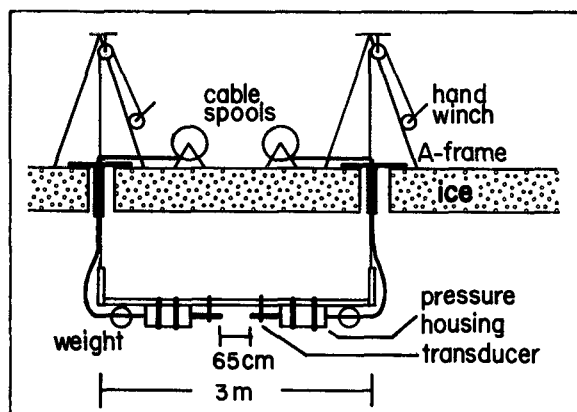


FIG. 2. Sketch of an underwater unit. Each unit comprised two transducers with accompanying electronics mounted on a steel bar that was suspended horizontally under the ice. The two adjacent transducers were used to measure scintillation drift and obtain horizontal velocity normal to the acoustic paths.

c. Transmit

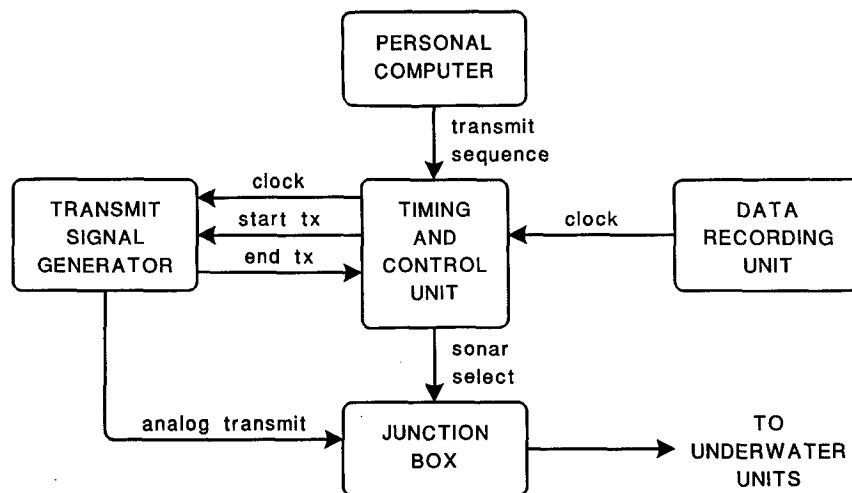
Transmission is initiated by downloading a transmission sequence from the personal computer to the timing and control unit (Fig. 3a). The transmission sequence most commonly used consisted of firing the transducers located at one corner of the array in quick succession, then waiting 200 ms for all direct and reflected paths to be received, and finally resetting all sonars before firing the next cluster of transducers. The entire cycle through all the transducers required 910 ms. Following each transmission, the sonars were reset so as to avoid effects of electronic interference on the clock signal.

Once the transmission sequence is downloaded, the timing and control unit takes over and the personal computer is available for other tasks. At the appropriate instant, the timing and control unit instructs the transmit-signal generator to start a transmission. The transmit-signal generator generates the analog transmit signal. An arbitrary waveform of up to 32 768 samples is stored in erasable, programmable read-only memory and played back under clock control. The signal then passes through a digital-to-analog converter and band-pass filter. One linear power amplifier is used for transmission. When the transmission is complete, the transmit-signal generator informs the timing and control unit and waits for the next instruction. The junction box contains relays that channel the output of the power amplifier to each transducer in succession as directed by the timing and control unit.

d. Sonars

Each sonar is designed to transmit, receive, digitize, and decode pseudorandom, phase-encoded acoustic signals using omnidirectional transducers that operate at a nominal frequency of 132 kHz (Fig. 4). The transmit-receive switch is of a simple design employing a dissipating resistor and a diode clamp at the input of the preamplifier. Pressure housings are located adjacent to each transducer. Each housing contains data acquisition, signal processing, and communications electronics. Data acquisition and digitizing are carried out with two 16-bit analog-to-digital converters that perform in-phase and quadrature sampling up to a maximum sampling rate of 50 kHz. During operation, a programmable gain amplifier is set to accommodate the acoustic signal level. The digitized data are decoded in real time by a vector signal processor that cross-correlates the received signal with a template of the code. A separate microprocessor serves as host to the signal processor, communicates with the surface electronics, and controls the operation of the data-acquisition board. In addition, this microprocessor formats the decoded data and sends a reduced dataset to the surface for storage.

a) transmit



b) receive

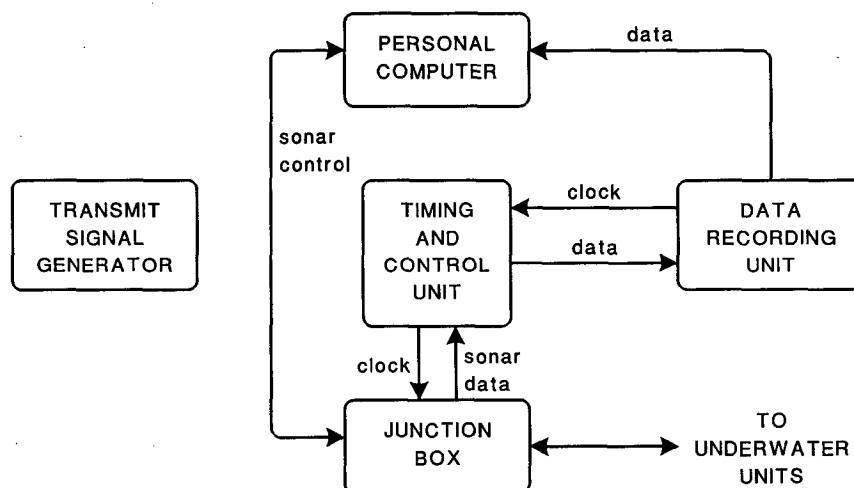


FIG. 3. Block diagram of the surface electronics. The surface modules are contained in a centrally located instrument hut and are responsible for the generation of the analog transmission signal, timing and control of the acoustic system, and storage and monitoring of the digital data collected by the sonars. The information and data flow between the units is illustrated during (a) transmission and (b) reception of acoustic signals.

e. Receive

The sonar data from all underwater units arrive at the surface on serial lines and are combined into a single data stream by the timing and control unit (Fig. 3b). The digital data are passed on to the recording unit at a sustained rate of 176.4 kB s^{-1} . This unit is made up of a date and time encoder, a pulse-code-modulation encoder, and videocassette recorders. The date and time encoder inserts timing information directly into the digital stream. In addition, timing in-

formation is continuously recorded on the audio channels of the video tapes. The pulse-code-modulation encoder is a consumer electronics device that converts a videocassette recorder into a high-fidelity digital audio recorder. We have modified the pulse-code modulator by bypassing its internal analog-to-digital converter so that it may accept digital instead of analog data. The video output is fed to two videocassette recorders allowing 16 h of autonomous operation. Each video tape has a total storage capacity of up to 5 GB (8 h) and is very cost effective (a fraction of a penny per megabyte).

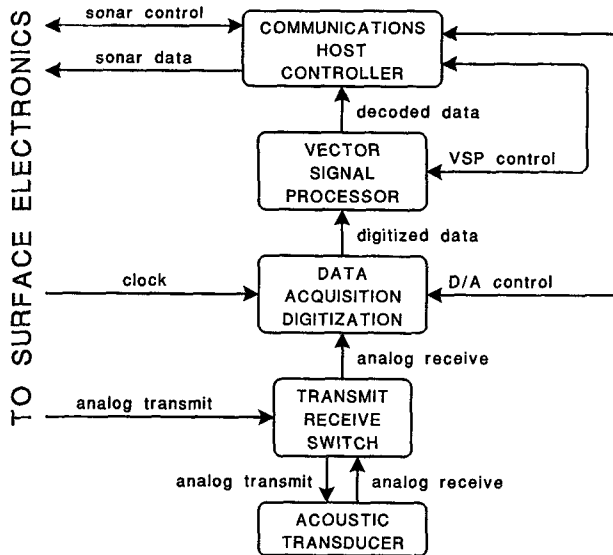


FIG. 4. Block diagram of the underwater units. Each sonar can transmit, receive, digitize, and decode pseudorandom, phase-encoded acoustic signals.

A personal computer is used to monitor data quality and to control the mode of operation of the sonars.

3. Processing

a. Encoding

The ice-ocean interface is a good reflector of sound. In order to ensure separation of the refracted and ice-reflected acoustic paths (Fig. 1), continuous wave transmission is not possible. Acoustic pulses must be used with width,

$$\tau_p < \frac{(l^2 + 4d^2)^{1/2} - l}{2c} \approx \frac{d^2}{cl}, \quad (1)$$

restricted by range l , depth d , and sound speed c . For example, a 90- μ s pulse permits a 200-m range, 5 m beneath the underside of the ice. A rule of thumb that has been used in radar work and related fields (Carlson 1986) is that the successful resolution of a bandpass pulse requires a system bandwidth β satisfying the inequality

$$\beta > \frac{1}{\tau_p} > \frac{cl}{d^2}. \quad (2)$$

The transmission signals were encoded both to reduce interference from other acoustic instruments deployed at the ice camp and to improve the precision of the signal amplitude and travel-time measurements, given the severe constraint on pulse width established by (1).

The coded signal consists of a binary modulation of the 132.3-kHz carrier by a 127-bit pseudorandom code that is a maximal linear sequence (Dixon 1984). The

binary transitions are keyed as 180° phase shifts of the carrier. Each bit is 12 carrier cycles long and has a period of 90.7 μ s. The complete sequence lasts 11.5 ms. Table 1 summarizes the code and digitizing parameters. A copy of the signal, sampled at 1.06 MHz and digitally prefiltered with a 22-kHz bandpass filter, is stored inside the transmit-signal generator. The 22-kHz bandwidth corresponds to the main lobe of the $[(\sin x)/x]^2$ sequence spectrum, contains 90% of the power in the overall signal, and comfortably satisfies (2).

The autocorrelation of a maximal linear sequence, obtained from an n -bit shift register, exhibits a triangular peak at zero lag, of height $2^n - 1$ and duration $2\tau_p$, where τ_p is the width of each bit. On each side of this peak, there are correlation sidelobes of length $(2^n - 2)\tau_p$. Figure 5 displays the autocorrelation function of the pseudorandom sequence used by the acoustic system. In multipath environments, the correlation sidelobes of a reflection may interfere with the peak of the direct path. The amount of interference depends on relative amplitude and delay between each path as a function of time. Under certain conditions, this interference establishes an upper bound on the signal-to-noise ratio of the system that cannot be exceeded even if the transmission power is increased. Depending on the experimental configuration and the multipath environment, the effects of sidelobe interference may be eliminated or minimized by changing the length of the code or adding guard sequences. It is also possible to remove the interference after the measurements are made. The correction is based on the known shape of the sidelobes, the linearity of the correlation operator, and the relative amplitude and location of each acoustic arrival.

b. Sampling and decoding

The sampling scheme recovers the in-phase $s_i(t)$ and quadrature $s_q(t)$ components of the acoustic signal relative to the carrier. In-phase samples are collected once every third carrier cycle at $f_s = f_c/3 = 44.1$ kHz, that is, four times per code bit. There is a $(4f_c)^{-1} = 1.89$ μ s delay between each in-phase and the corresponding quadrature sample. This digitizing scheme effectively

TABLE 1. Coded sequence and digitizing parameters.

Parameter	Value
Carrier frequency f_c (kHz)	132.3
Acoustic signal bandwidth β (kHz)	22
Phase shift used for coding (°)	180
Digital sampling rate f_s (kHz)	44.1
Bit period τ_p (μ s)	90.7
Carrier cycles per bit	12
Digital samples per bit	4
Sequence length (bits)	127
Sequence length T (ms)	11.5

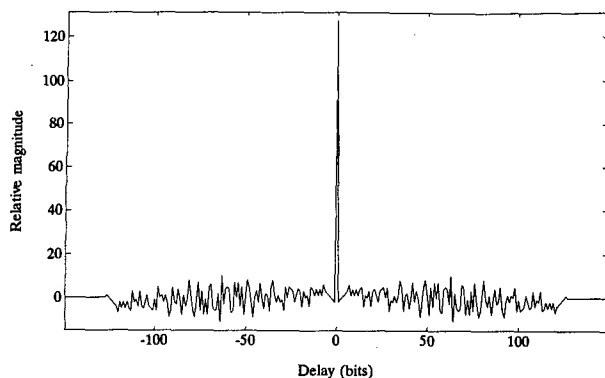


FIG. 5. Autocorrelation of the pseudorandom sequence used by the acoustic system. The code is generated using a 7-bit shift register. The autocorrelation function exhibits a triangular peak at zero lag, of height $2^7 - 1$ and duration $2\tau_p$, where τ_p is the width of each bit. On each side of this peak, there are correlation sidelobes with peak amplitude smaller than $(2^7 - 1)^{1/2}$ and duration $(2^7 - 2)\tau_p$.

mixes down a 44.1-kHz bandpass signal centered at $f_c = 132.3$ kHz to a 22-kHz low-pass equivalent. This bandwidth is twice that of the acoustic signal; therefore, the code information is preserved. The amplitude $A(t)$ and phase $\phi(t)$ of the signal may be recovered from

$$A(t) = [s_i^2(t) + s_q^2(t)]^{1/2} \quad (3)$$

and

$$\phi(t) = \arctan \frac{s_q(t)}{s_i(t)} \quad (4)$$

as a function of time t .

During normal operation, real-time decoding of the digitized acoustic signals is accomplished at each sonar by the vector signal processor. An unfiltered copy of the code, sampled at 44.1 kHz, is used as a decoding template, and short guard sequences are appended on either side. In-phase and quadrature samples are continuously correlated with this template. The *overlap-save* method (Press et al. 1986) is used for performing fast correlation in the frequency domain. The signal processor also computes magnitude squared and low-pass-filtered time series. Synchronization between transmission and reception is achieved by using a common clock. The process gain G is a function of bandwidth β and the total length of the sequence T :

$$G = 10 \log \beta T = 24 \text{ dB}. \quad (5)$$

Finally, it must be noted that the quadrature sampling scheme increases the signal-to-noise ratio by an additional 3 dB over and above the process gain defined by (5).

c. Reduction, storage, and monitoring

The communications processor, contained in each sonar, is programmed to initialize, test, and monitor the data-acquisition electronics and the vector signal

processor and to communicate with the surface. Under normal operation, it locates four peaks in each block of data. For each set of 512 complex 16-bit samples, 85 data words are produced that preserve most of the useful information contained in the decoded signal. This results in a data-reduction rate of 12:1, thereby decreasing the required storage bandwidth.

The reduced data from all the sonars are multiplexed into a single data stream at the surface and stored on video tapes. A personal computer is used to monitor data quality. During data collection, short samples are written on to disk and subsequently analyzed to verify correct operation of the acoustic system. When the system is not actively monitored by the operator, a background program is used to continuously sample the data and to correct irregularities and malfunctions.

d. Correlation peak interpolation

During postprocessing, the data is processed in two steps. First, each tape is read at the same rate at which it was written using a pulse-code-modulation encoder and personal computer. For specified acoustic paths, the location and amplitude of the correlation peaks are obtained using the scheme described in this section. In a typical run, the program will read a 5-GB (8-h) tape, create a 20-MB file containing information about two dozen acoustic paths, and store this information on erasable optical disk cartridges. A second computational pass is required to convert these data files into time series of amplitude, travel time, path-averaged velocity, and relative vorticity, as discussed in the next section.

Peak location and amplitude must be interpolated from five data points surrounding the top of each peak. The phase of the acoustic arrival relative to that of the transmitted signal is then used as a vernier scale to improve the estimate of location to within a fraction of a carrier cycle. There is an inherent 360° ambiguity in the measurement of phase using (4). Therefore, the interpolation scheme must estimate peak location within half a carrier cycle using data points that are spaced three carrier cycles apart (Table 1). The problem is further complicated by the presence of noise and the necessity of implementing the algorithm on data being read at a sustained rate of 176.4 kB s^{-1} .

As discussed earlier, the correlation peak exhibits a triangular shape that has a width equivalent to two code bits, or in this case, eight data points. The simplest solution for the interpolation problem is a triangular fit through the five recorded data points surrounding each peak. The limited system bandwidth smooths the peak, so that this approach does not provide the required accuracy.

Gupta and Painter (1966) show that the cross correlation between input x and output y of a system may be expressed as

$$R_{yx}(\tau) = h(\tau) * R_{xx}(\tau), \quad (6)$$

where the convolution of the impulse response $h(\tau)$ with the autocorrelation function of the input signal $R_{xx}(\tau)$ is a function of delay $\tau = t - t_0$, where t_0 is the location of the peak. To a good approximation, the acoustic system is characterized by a band-limited frequency response,

$$\mathcal{H}(f) = \begin{cases} 1, & \text{if } -\tau_p^{-1} \leq f \leq \tau_p^{-1} \\ 0, & \text{otherwise,} \end{cases} \quad (7)$$

where $\mathcal{H}(f)$ is the Fourier transform of $h(\tau)$. The coded sequence has a triangular autocorrelation function

$$R_{xx}(\tau) = \begin{cases} A(1 + \tau/\tau_p), & \text{for } -\tau_p \leq \tau < 0 \\ A(1 - \tau/\tau_p), & \text{for } 0 \leq \tau \leq \tau_p \\ 0, & \text{otherwise.} \end{cases} \quad (8)$$

We solve this set of equations to obtain an expression for the shape of the cross-correlation peak,

$$R_{yx}(t) = A \sum_{n=0}^{\infty} a_n \left(\frac{t - t_0}{\tau_p} \right)^{2n}, \quad (9)$$

a polynomial with coefficients a_n . The amplitude A and location t_0 are determined from the five recorded data points surrounding the correlation peak using a nonlinear curve-fitting algorithm (appendix A). This second approach gives optimal accuracy but could not be implemented at the required data rate using the available hardware.

In between these two extremes, there exist a number of other approaches representing a compromise between accuracy and computational complexity. We used linear least squares to fit the five data points to a quadratic,

$$R_{yx}(t) = A_q \left[1 - \left(\frac{t - t_0}{B} \right)^2 \right], \quad (10)$$

where $2B$ is the width of the peak at its base, A_q the amplitude, and t_0 the location (appendix A).

e. Velocity and vorticity evaluation

The second computational pass converts data files into time series of amplitude, travel time, path-averaged velocity, and relative vorticity. Velocity is obtained using reciprocal travel-time difference. The travel time from point P_1 to P_2 is

$$t_{12} = \frac{l_{12}}{\bar{c}_{12} + \bar{u}_{12}}, \quad (11)$$

where \bar{c}_{12} and \bar{u}_{12} are the path-averaged sound speed and fluid velocity, respectively, along the ray joining P_1 with P_2 , and l_{12} is the range. Assuming that \bar{c}_{12} , \bar{u}_{12} , and l_{12} remain momentarily unchanged, the travel time in the reciprocal direction is

$$t_{21} = \frac{l_{12}}{\bar{c}_{12} - \bar{u}_{12}}, \quad (12)$$

and the travel-time difference is

$$\Delta t_{12} = t_{21} - t_{12} = \frac{2\bar{u}_{12}l_{12}}{\bar{c}_{12}^2 - \bar{u}_{12}^2} \approx \frac{2\bar{u}_{12}l_{12}}{\bar{c}_{12}^2}, \quad (13)$$

since $u \ll c$. The sum of the reciprocal travel times $\sum t_{12} = t_{12} + t_{21}$ is used to eliminate either l_{12} or c_{12} from (13) and solve for the path-averaged velocity,

$$\bar{u}_{12} = \frac{\Delta t_{12}}{\sum t_{12}} \bar{c}_{12} \approx \frac{2\Delta t_{12}}{(\sum t_{12})^2} l_{12}. \quad (14)$$

Vorticity is obtained using the method proposed by Rossby (1975). The line integral of fluid motion between points P_1 and P_2 can, under the assumptions made above, be written as

$$\int_{P_1}^{P_2} \mathbf{u} \cdot d\mathbf{s} = \bar{u}_{12}l_{12} = \frac{\bar{c}_{12}^2}{2} \Delta t_{12}, \quad (15)$$

where \mathbf{u} is the velocity vector and \mathbf{s} is a unit vector along the acoustic propagation path. Thus, the line integral around triangle $P_1P_2P_3$ becomes

$$\oint \mathbf{u} \cdot d\mathbf{s} = \bar{u}_{12}l_{12} + \bar{u}_{23}l_{23} + \bar{u}_{31}l_{31} \\ = \frac{\bar{c}_{12}^2}{2} \Delta t_{12} + \frac{\bar{c}_{23}^2}{2} \Delta t_{23} + \frac{\bar{c}_{31}^2}{2} \Delta t_{31}. \quad (16)$$

From Stoke's theorem, the circulation is equivalent to the surface integral of the normal component of vorticity. If the triangle lies on a horizontal plane, this is the product of the average vertical component of relative vorticity $\bar{\zeta}_z$, with the area of the triangle A_T :

$$\oint \mathbf{u} \cdot d\mathbf{s} = \int \int (\nabla \times \mathbf{u})_z dx dy = \bar{\zeta}_z A_T. \quad (17)$$

Assuming that $\bar{c}_{12} \approx \bar{c}_{23} \approx \bar{c}_{31} \approx \bar{c}$, (16) and (17) yield

$$\bar{\zeta}_z \approx \frac{\bar{c}^2}{2A_T} (\Delta t_{12} + \Delta t_{23} + \Delta t_{31}). \quad (18)$$

A consequence of the above equation is that for a desired resolution in vorticity, the travel-time difference must be measured with a precision that increases in inverse proportion to the square of the dimension of the acoustic array.

4. Observations

The oceanographic objective of the Coordinated Eastern Arctic Experiment (CEAREX) was to measure the processes responsible for the exchange of heat, mass, and momentum between the Arctic Ocean and the atmosphere. A camp was established on 18 March 1989, 300 km northwest of Spitsbergen, and drifted with the pack ice for six weeks (Padman and Dillon 1991). The six underwater units were deployed at two separate depths at the vertices of an equilateral triangle with

sides of length 201, 205, and 211 m; the acoustic array was laid out beneath the floe so as to span both multiyear and young ice, thus providing contrasting turbulence regimes (Fig. 6).

a. Sources of error

For the derivation of (14) and (18), it was assumed that sound speed and flow field, along the acoustic propagation paths, do not change during the time required for reciprocal transmission. Although this assumption is only an approximation, we found that in the turbulent boundary layer beneath the ice camp the effect of spatial and temporal variance on measurement accuracy was small compared to other sources of error.

In the presence of shear, an error is caused by lack of reciprocity of the acoustic paths. It can be shown that for vertical shear σ , range l , and sound speed c , the sum of the reciprocal travel times is decreased by $\sigma^2 l^3 / 24 c^3$, and the maximum separation between the reciprocal rays is $\sigma l^2 / 4 c$ (appendix B). For $\sigma = 10^{-3} \text{ s}^{-1}$, $l = 200 \text{ m}$, and $c = 1440 \text{ m s}^{-1}$, the error in the total travel time ($\approx 112 \text{ ps}$) and the maximum separation between the reciprocal acoustic paths ($\approx 7 \text{ mm}$) are insignificant.

A significant error may be caused by vertical shear if the array is not horizontal. Consider a shear-induced horizontal vorticity component

$$\zeta_x = \frac{\partial w}{\partial y} - \frac{\partial v}{\partial z} \quad (19)$$

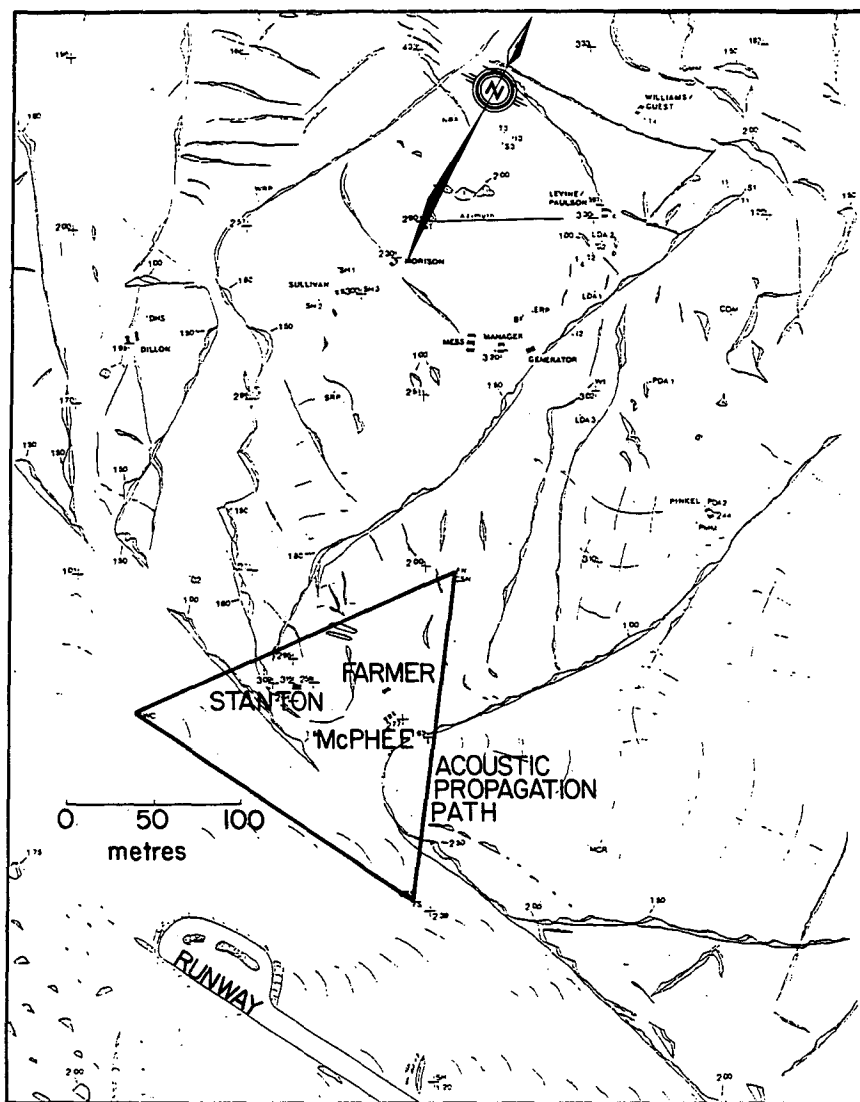


FIG. 6. Aerial view of CEAREX oceanography ice camp. The camp was located on multiyear ice as indicated by the large number of pressure ridges. The underwater units of the acoustic system were deployed at the corners of the triangle drawn on the diagram. The array is seen to span both first-year and multiyear ice (ice map courtesy of Robin Williams).

in an orthogonal coordinate system xyz . In a rotated coordinate system $x'y'z'$, there is an apparent vertical vorticity component

$$\zeta_{z'} = -\zeta_x \sin\theta, \quad (20)$$

where θ is the angle between axis z and z' . For example, a typical vertical shear $\partial v/\partial z = 10^{-3} \text{ s}^{-1}$ will cause an apparent vertical vorticity $\zeta_{z'} = 10^{-6} \text{ s}^{-1}$, less than 1% of the planetary vorticity, for an inclination $\theta = 3'30''$. This angle is equivalent to a 20-cm depth misalignment of the array over 200 m. The uncertainty in the depth of the moorings during deployment was less than ± 2 cm. Depth misalignment may also have occurred during the experiment because of the swinging motion of the moorings. The amplitude of the relative mooring motion at the 20-m depth was less than 20 cm. This corresponds to a worst-case relative change in depth of 1 mm. Therefore, the expected error due to misalignment of the acoustic elements is less than 0.1% of the planetary vorticity.

The accuracy of the acoustic measurements is limited by interference from the multipath environment. During the experiment, we found that the acoustic signal reflected by the ice was of comparable strength to the direct path. Under the smooth ice of the newly refrozen lead, the reflected path was at times 20%–30% stronger than the direct path. The smoothly varying surface of the underside of the ice can, under certain circumstances, behave like a large concave mirror that focuses acoustic energy. Mooring motions bring the transducers in and out of acoustic focus relative to each other. As discussed in section 3a, interference from the correlation sidelobes of the ice-reflected acoustic paths establishes an upper bound on the signal-to-noise ratio that can be achieved by the acoustic system.

Mooring motions during the measurement time frame introduce an error δt in reciprocal travel-time difference. The magnitude of this error as a function of angular frequency $\omega = 2\pi f$ is bounded by

$$\delta t(\omega) \leq \frac{\omega M(\omega) \tau_{tr}}{c}, \quad (21)$$

where $M(\omega)$ is the amplitude of the relative mooring motion and τ_{tr} is the delay between transmission and reception of a reciprocal pair of pulses. From (21), it follows that the error introduced by mooring motion has zero average and is limited to the high-frequency end of the spectrum. For this reason, the moorings were designed so as to minimize strumming and high-frequency oscillations.

b. Amplitude scintillation

Acoustic energy propagating through a random medium is modulated by spatial and temporal fluctuations in the refractive index that give rise to intensity and phase fluctuations on a receiving plane. The structure and movement of this time-varying scintillation pattern

can be interpreted in terms of the structure and motion of the intervening fluid.

In Fig. 7 we compare time series of log amplitude $\chi(t) = \ln[A(t)/\langle A(t) \rangle]$ for two parallel horizontal acoustic paths of length $l = 211$ m, orientation 344°T , and depth 8.4 m; $A(t)$ is the amplitude of the received signal, and the angle brackets indicate an ensemble average. The two paths are separated by $r = 56.3$ cm, approximately one third of the Fresnel zone size, $(\lambda l)^{1/2} = 1.52$ m. During the time of the measurement, the mean flow relative to the ice at 8.4-m depth has speed 11 cm s^{-1} and direction 55°T ; therefore, the component of flow perpendicular to the acoustic paths is $U_\perp = 10.4 \text{ cm s}^{-1}$.

Four-minute time series of $\chi(t)$ obtained on 18 April 1989 for the upstream and downstream acoustic paths are displayed in Figs. 7a and 7b, respectively. The time series are noisy, and there appears to be little correlation between the two. Segments of the lognormalized sound intensity of 256-points length are Fourier transformed and normalized by the Fresnel translation frequency $f_0 = U_\perp(2\pi\lambda l)^{-1/2}$, in order to determine the spectral properties of the time series. In Fig. 7c we display a 7-h average of the acoustic log-amplitude power spectrum $\Gamma_\chi(f)$ for the upstream acoustic path normalized by f/f_0 so as to allow direct comparison with Fig. 9 of Farmer et al. (1987). The dotted lines enclose the 95% confidence interval of the spectrum. The dashed line is a constant fitted to the high-frequency noise floor. We attribute this noise to interference from the ice-reflected acoustic signal. Though the measurements are an order of magnitude more sensitive than those made by Farmer et al. in Cordova Channel, we do not observe the peak at the Fresnel wavenumber predicted by the propagation theory. This may be explained by the much weaker refractive-index variability in the ice-water boundary layer.

In Fig. 7d, we plot the coherence function between the log-amplitude spectra of the two adjacent acoustic paths. For $f/f_0 > 6$, the two time series are uncorrelated; at lower frequencies there is some coherence between the two time series. This indicates that a certain percentage of the observed fluctuations are caused by refractive-index fine structure that remains coherent as it is advected past the two acoustic paths. We low-pass filter the log-amplitude time series to remove what is known to be measurement noise and plot the resulting time series and spectrum as solid lines in Figs. 7a–c.

In Figs. 7e and 7f, we plot the normalized log-amplitude autocovariance and cross covariance of the filtered time series for the 4-min segments displayed in Figs. 7a and 7b. Because the high-frequency end of the spectrum is missing, the width of the autocovariance peak at zero lag has no physical significance; it depends on the characteristics of the applied filter. For the same reason, the slope at zero lag of the cross covariance cannot be used to determine flow speed. There is, however, some similarity between the autocovariance function of the two paths, which indicates that the re-

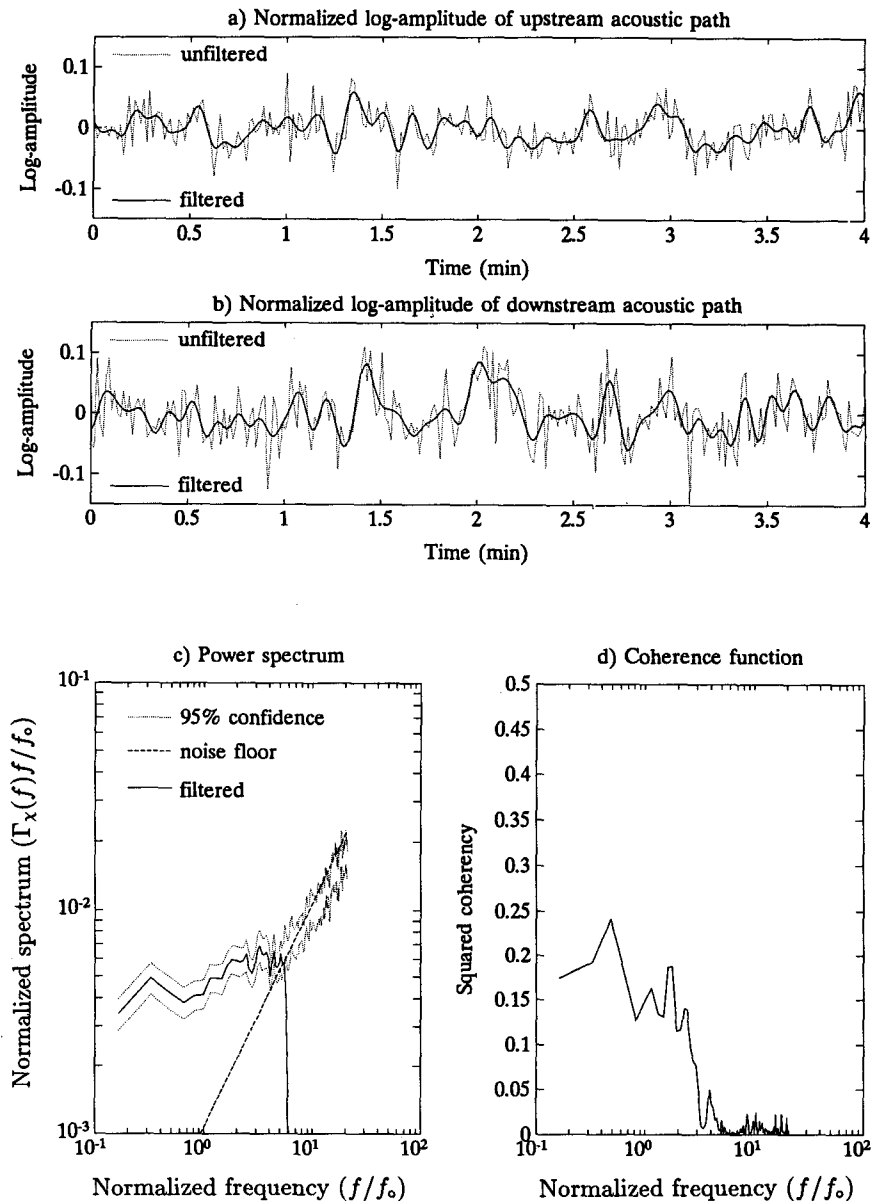


FIG. 7. Comparison of log-amplitude time series for two adjacent horizontal acoustic paths. (a) Normalized log amplitude $\chi(t)$ of the upstream acoustic path, length $l = 211$ m, orientation 344° T, and depth 8.4 m. (b) $\chi(t)$ for the adjacent parallel acoustic path located $r = 56.3$ cm downstream of the first path. (c) Normalized spectrum $\Gamma_X(f)/f/f_0$ of the upstream acoustic path. (d) Squared coherency between the two paths. (e) Autocovariance of the two paths. (f) Cross covariance between the two paths.

fractive index fine structure remains somewhat coherent as it is advected past the two parallel acoustic paths. Therefore, we may use delay to the peak of the cross-covariance function, $\tau_p = -4.7$ s, to estimate the horizontal velocity component normal to the acoustic paths, $U_\perp = -r/\tau_p = 12$ cm s $^{-1}$.

Figure 8 shows time series of horizontal velocity determined using τ_p along one side of the triangular array and velocity obtained using reciprocal transmission along the other two sides of the array. The velocity

estimates are based on 20- and 40-min time series. Despite the limitations of eddy decay, a flow-dependent weighting function, and the difficulty in measuring small currents using the peak-delay processing scheme, the measurements shown here demonstrate the viability of the scintillation technique for use in the ice-water boundary layer.

The signal-to-noise ratio was dominated by interference from the ice-reflected path. A modest change, however, in data recording (i.e., continuously recording

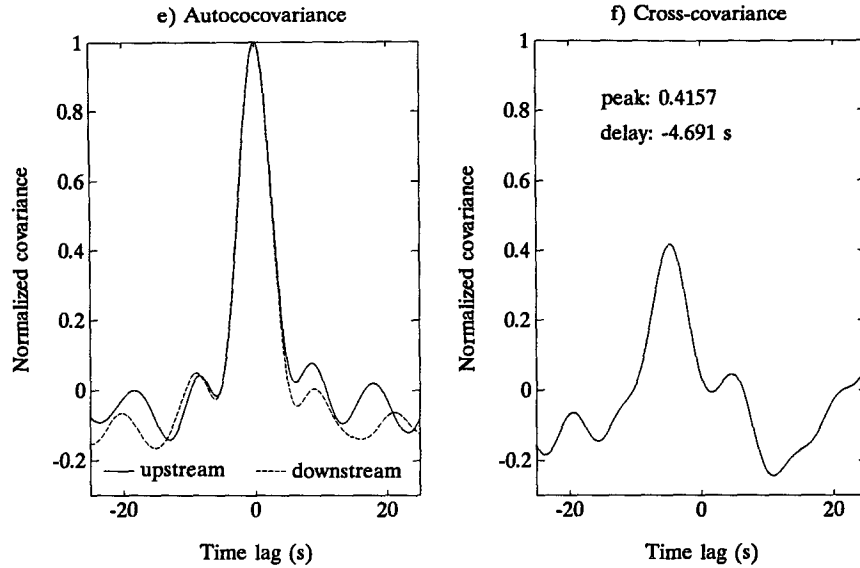


FIG. 7. (Continued)

both the direct and reflected arrivals, or including longer guard sequences as detailed in section 3a) would have greatly improved results, allowing accurate scintillation flow measurements based on the full spectrum.

c. Travel time

Acoustic travel time between transducers is measured to within a small fraction of the carrier period ($\tau_c = 7.56 \mu\text{s}$) by first interpolating the location of the transmit and receive peaks to resolve the phase ambiguity and subsequently using phase to provide high-resolution measurements. An unfiltered 20-min time

series of travel time between two transducers located at a depth of 8 m is shown in Fig. 9. The average value of 146.83 ms indicates a mean separation of 211 m. The oscillations are principally caused by relative mooring motion resulting in displacements of up to 4 cm in this short data section.

The spectrum of acoustic travel time for an 8-h time series, which includes the section of data of Fig. 9, is shown in Fig. 10. At high frequency, there is a white noise floor at a level of $7 \times 10^{-3} \mu\text{s}^2 \text{Hz}^{-1}$. We attribute this noise floor to multipath interference with line-of-sight reception. For decreasing frequency, the spectral density sharply rises to $1.5 \mu\text{s}^2 \text{Hz}^{-1}$ at $\omega_r/2\pi = 0.133$

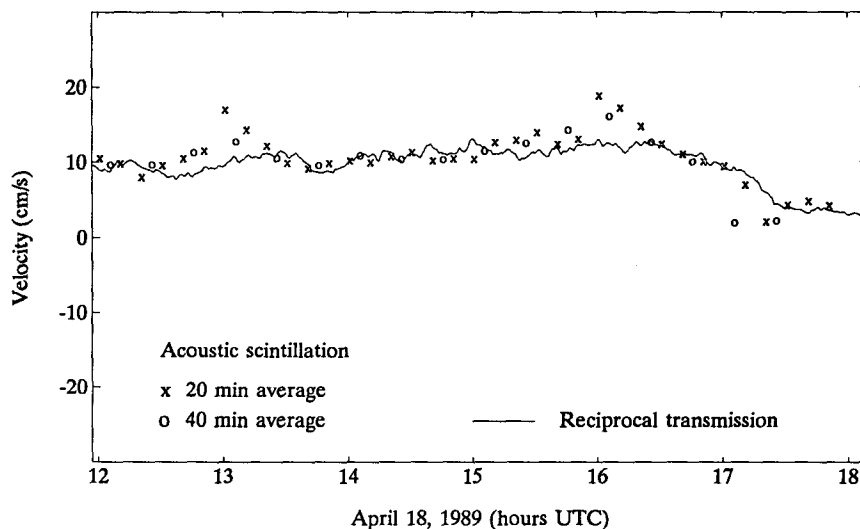


FIG. 8. Time series of horizontal velocity determined using delay to the peak of the cross-covariance function, τ_p , compared to velocity measurements obtained using reciprocal transmission.

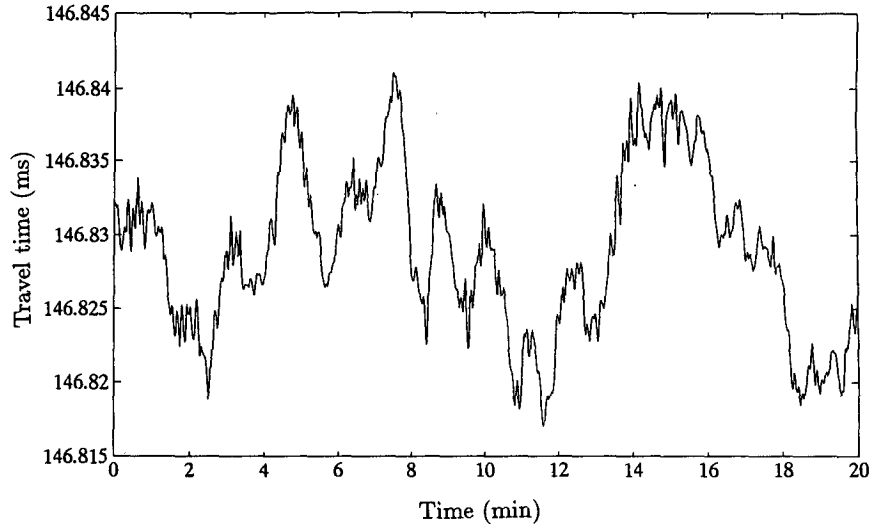


FIG. 9. Acoustic travel time between two transducers at the 8-m depth, separated by 211 m in a direction of 344°T , for data collected in the boundary layer on 18 April 1989. The oscillations are a result of relative mooring motion and correspond to displacements of up to 4 cm.

Hz, which is the mechanical resonance frequency of the 8-m moorings. At still lower frequency, the power spectral density increases more gradually.

Relative mooring motion can be determined by analyzing the travel time of acoustic pulses. To a first approximation, each mooring behaves as a damped pendulum oscillator with a forcing term introduced by currents beneath the ice. For small displacements, and linear damping, the horizontal motion of a forced pendulum is controlled by

$$\frac{d^2x}{dt^2} + 2\gamma \frac{dx}{dt} + \omega_0^2 x = \frac{F(\omega_f)}{m} \cos \omega_f t, \quad (22)$$

where γ is the damping constant, $\omega_0 = (g/d)^{1/2}$ the natural angular frequency, m the mass, ω_f the forcing frequency, and $F(\omega_f)$ the forcing term (Alonso and Finn 1967). The flow field provides forcing, and the system oscillates with amplitude

$$M(\omega_f) = \frac{F(\omega_f)/m}{[(\omega_f^2 - \omega_0^2)^2 + 4\gamma^2 \omega_f^2]^{1/2}}, \quad (23)$$

which is equal to $F(\omega_f)/m\omega_0^2$ at low frequencies, has a local maximum at the mechanical resonance frequency $\omega_r = (\omega_0^2 - 2\gamma^2)^{1/2}$, and varies as $F(\omega_f)/m\omega_f^2$ at high frequencies.

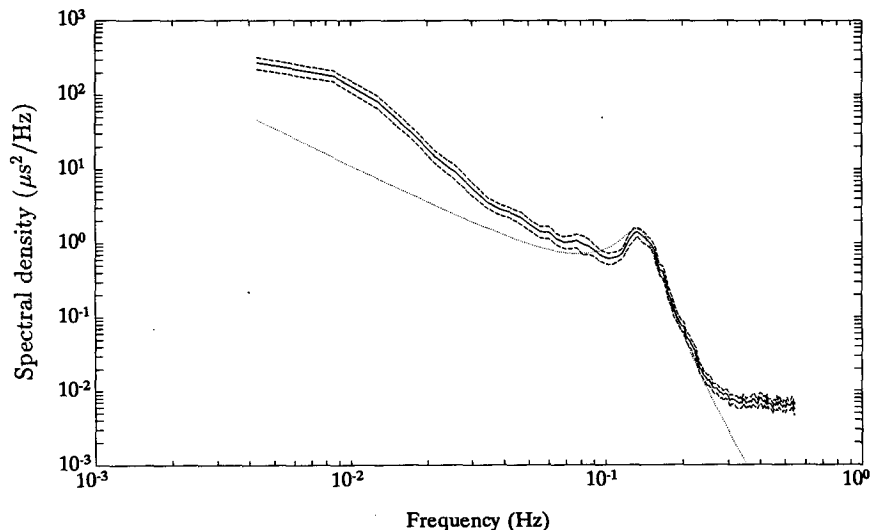


FIG. 10. Acoustic travel-time power spectrum at 8-m depth. The data consist of an 8-h time series sampled at 1.1 Hz on 18 April 1989. The dashed lines enclose the 95% confidence interval. The dotted line is a theoretical prediction of mooring motion.

In addition to simple swinging, the moorings have a rotational mode of oscillation (Fig. 2). The natural frequency of rotation decreases down to a minimum of $\omega_0 = (g/d)^{1/2}$, as the weights are moved toward the edges of the suspended steel bars. We neglect this mode of oscillation for two reasons. First, the transducers are centered on the iron bar; therefore, their position relative to other moorings depends primarily on swinging rather than on rotation. Second, most of the weight is concentrated at the edges of the steel bars; therefore, the natural swinging and rotational frequency are almost equal and their spectral signatures on one-way travel time are indistinguishable.

We assume that the mooring motions of the transmitting and receiving transducers are statistically independent, which is certainly true at sufficiently high frequency. Therefore, the spectral contributions to travel time from the motion of the two moorings add up algebraically. The dotted line in Fig. 10 is a theoretical prediction of the spectrum, obtained using (23) and a Kolmogorov inertial subrange forcing term $F^2(\omega_f) = F_0^2 \omega_f^{-5/3}$. The natural frequency of oscillation ω_0 and the forcing constant F_0 are chosen to optimize the fit between data and theory at high frequency. The model successfully predicts the steep $-17/3$ spectral slope at high frequency and the presence of a local maximum in the spectrum due to mechanical resonance of the moorings.

At low frequency, the inertial subrange approximation does not hold and we expect a spectral slope that is less steep than $-5/3$. Instead, the model underestimates the spectral intensity. In addition, the natural frequency used to fit the model to the data, $\omega_0/2\pi = 0.14$ Hz, is lower than $(g/d)^{1/2} = 0.17$ Hz, the expected frequency based on deployment depth. We at-

tribute these discrepancies to the nonlinear dependence between the forcing and damping terms, and the flow field.

d. Path-averaged current

1) ACCURACY

Path-averaged current measurements are based on travel-time difference of reciprocal acoustic propagations. Therefore, the accuracy of the current measurement is ultimately limited by the precision with which travel time can be measured in both directions. Another factor limiting the accuracy of the measurements is relative mooring motion, as discussed in section 4a.

Figure 11 displays the power spectral density of path-averaged velocity measurements obtained at 8-m depth for the same 8-h period as Fig. 10. At high frequency, there is a white noise floor at a level of $5 \times 10^{-3} \text{ cm}^2 \text{ s}^{-2} \text{ Hz}^{-1}$, which corresponds to the combined noise floor of the two reciprocal travel-time measurements. Near the mechanical resonance frequency of the moorings, the error introduced by relative motion during a reciprocal transmission dominates the velocity measurements. The power spectral density of the error due to mooring motion is estimated using (21) and drawn as a dotted line on the figure. Clearly, the peak in the spectral density at 0.133 Hz is caused by relative mooring motion. For frequencies lower than 0.07 Hz, the error caused by mooring motion drops below the spectral level of path-averaged currents.

An alternative analysis of mooring-motion effects is based on the coherence function between the power spectra of one-way travel time and velocity, shown in

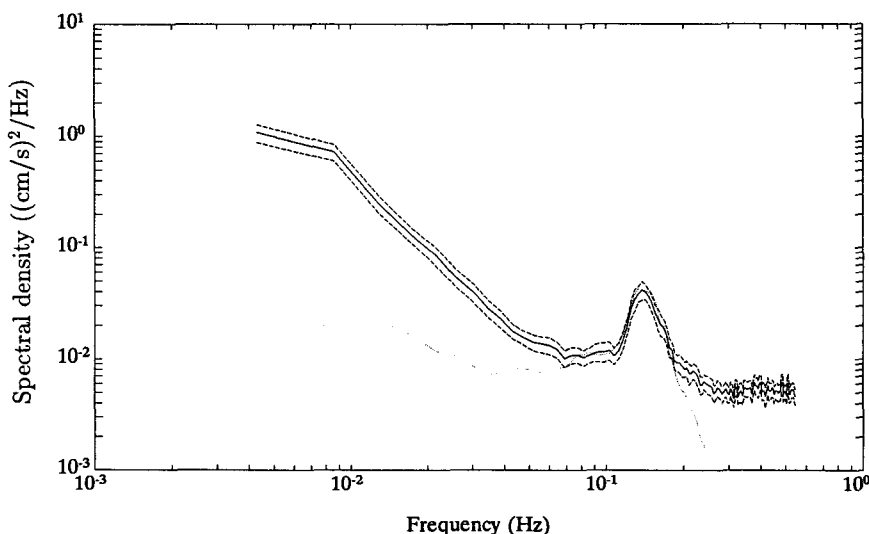


FIG 11. Power spectrum of path-averaged velocity measurements at the 8-m depth, for the same 8-h period as Fig. 10. The dashed lines enclose the 95% confidence interval. The dotted line is an estimate of error due to relative mooring motion during a reciprocal transmission.

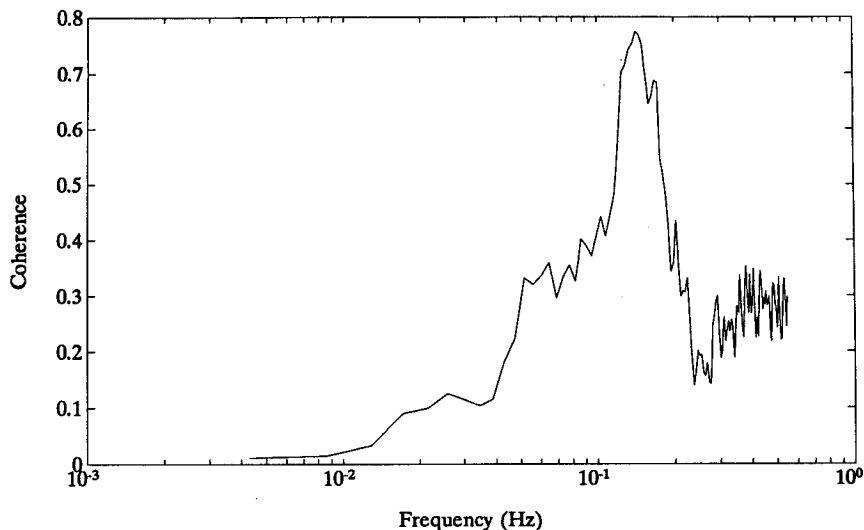


FIG. 12. Squared coherency function between power spectra of one-way travel time and velocity at the 8-m depth, for the same 8-h period as Fig. 10.

Fig. 12. The coherence of the two signals is high in the neighborhood of mechanical resonance; at frequencies below 0.07 Hz, low coherence confirms that mooring motion is not an important factor. All velocity and vorticity data is low-pass filtered to remove the error due to mooring motion. Assuming Gaussian white noise with a spectral density of $5 \times 10^{-3} \text{ cm}^2 \text{ s}^{-2} \text{ Hz}^{-1}$, equivalent to that observed at high frequency, the rms noise level is less than 0.1 mm s^{-1} at a filtered sampling rate of once per minute.

2) PATH-AVERAGING FILTER CHARACTERISTICS

The acoustic array behaves as a path-averaging filter that damps turbulent velocity fluctuations and focuses on low wavenumbers. Given a sinusoidal disturbance $A \cos(\mathbf{k} \cdot \mathbf{x} - \omega t)$ superimposed on mean flow \mathbf{U} , the velocity field relative to the ice is

$$\mathbf{u} = \mathbf{U} + A \frac{\mathbf{k}}{k} \cos[\mathbf{k} \cdot \mathbf{x} - (\omega + \mathbf{k} \cdot \mathbf{U})t], \quad (24)$$

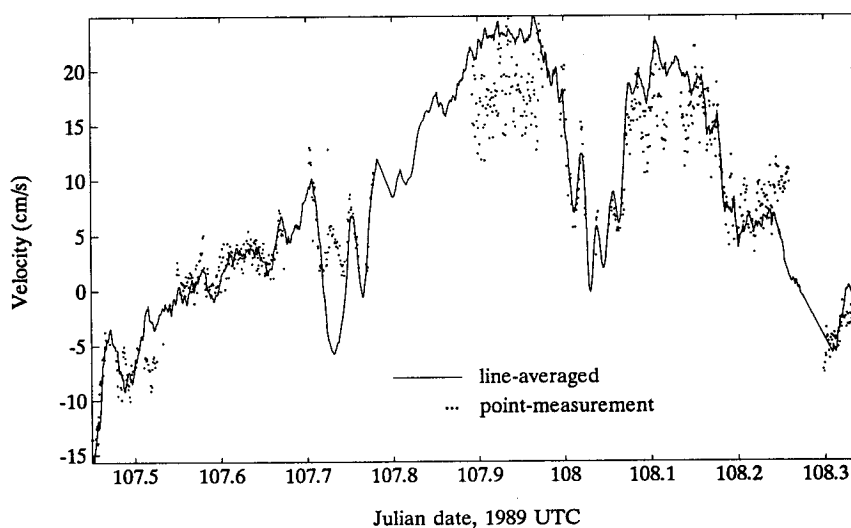


FIG. 13. Comparison between path-averaged and point current measurements. The solid line is a velocity time series obtained with the acoustic current meter at the 8.4-m depth, 344°T , on 17 and 18 April 1989. A 0.0083-Hz low-pass filter has been applied to the data. The dots are 1-min averages from a mechanical current meter that has a spatial resolution of 20 cm; the current meter was located in the center of the acoustic array at a depth of 10.4 m.

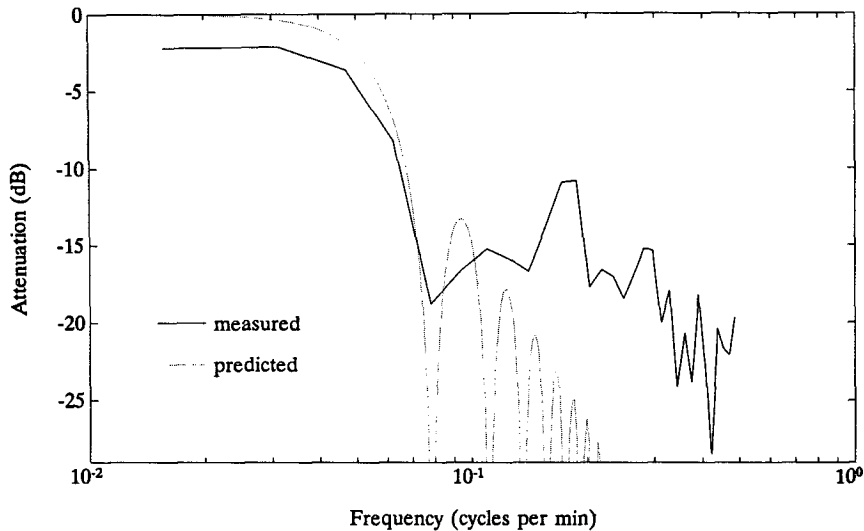


FIG. 14. Magnitude of the transfer function between the path-averaged and point measurements of Fig. 13. The dotted line is a theoretical prediction based on the spatial resolution of the acoustic array and a two-layer fluid internal-wave-dispersion relation.

where $k = 2\pi/\lambda$ is the wavenumber, \mathbf{k}/k is a unit vector parallel to the wave vector, and $\mathbf{k} \cdot \mathbf{U}$ is the Doppler shift caused by the motion of the measuring frame relative to the sinusoidal disturbance. We consider velocity averaged along baseline l ,

$$\begin{aligned} \tilde{u}(\mathbf{x}, t) &= \frac{1}{l} \int_{-l/2}^{l/2} \mathbf{u}(\mathbf{x}, t) \cdot d\mathbf{x} \\ &= \frac{\mathbf{U} \cdot \mathbf{l}}{l} + \frac{2A}{kl} \sin(\mathbf{k} \cdot \mathbf{l}/2) \cos[(\omega + \mathbf{k} \cdot \mathbf{U})t], \end{aligned} \quad (25)$$

so that for events coherent along the acoustic propagation path, the response of the system is

$$H(k) = \frac{\sin(\mathbf{k} \cdot \mathbf{l}/2)}{\mathbf{k} \cdot \mathbf{l}/2}, \quad (26)$$

where $l \approx 200$ m is the range between the array elements. This is a low-pass filter with a cutoff wavelength of $\lambda_0 \approx 450$ m and zero phase shift in the passband.

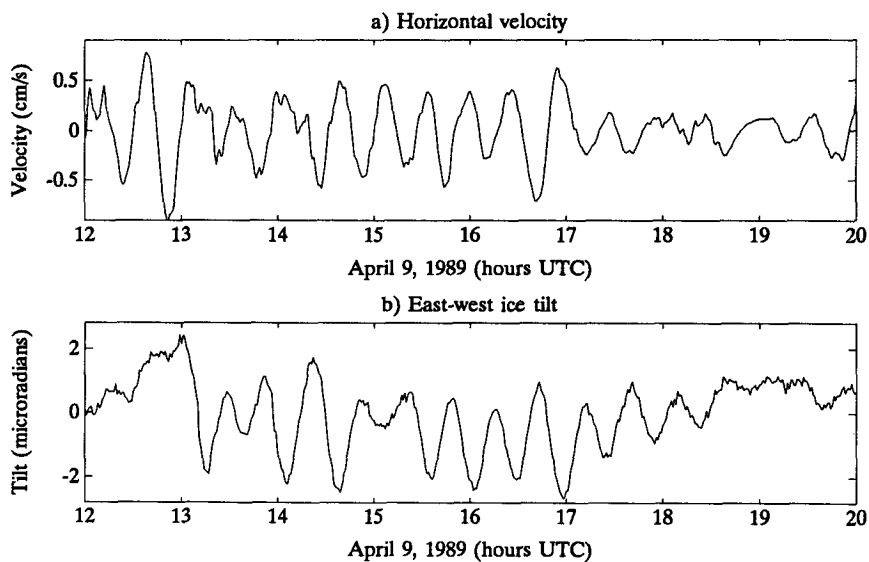


FIG. 15. Low-amplitude wave train. (a) Current speed relative to the ice at 20.4-m depth. The time series is filtered with 0.0083-Hz low-pass and 1-cph high-pass filters. (b) East-west ice tilt. The tiltmeter and the acoustic array were separated by some 337 m.

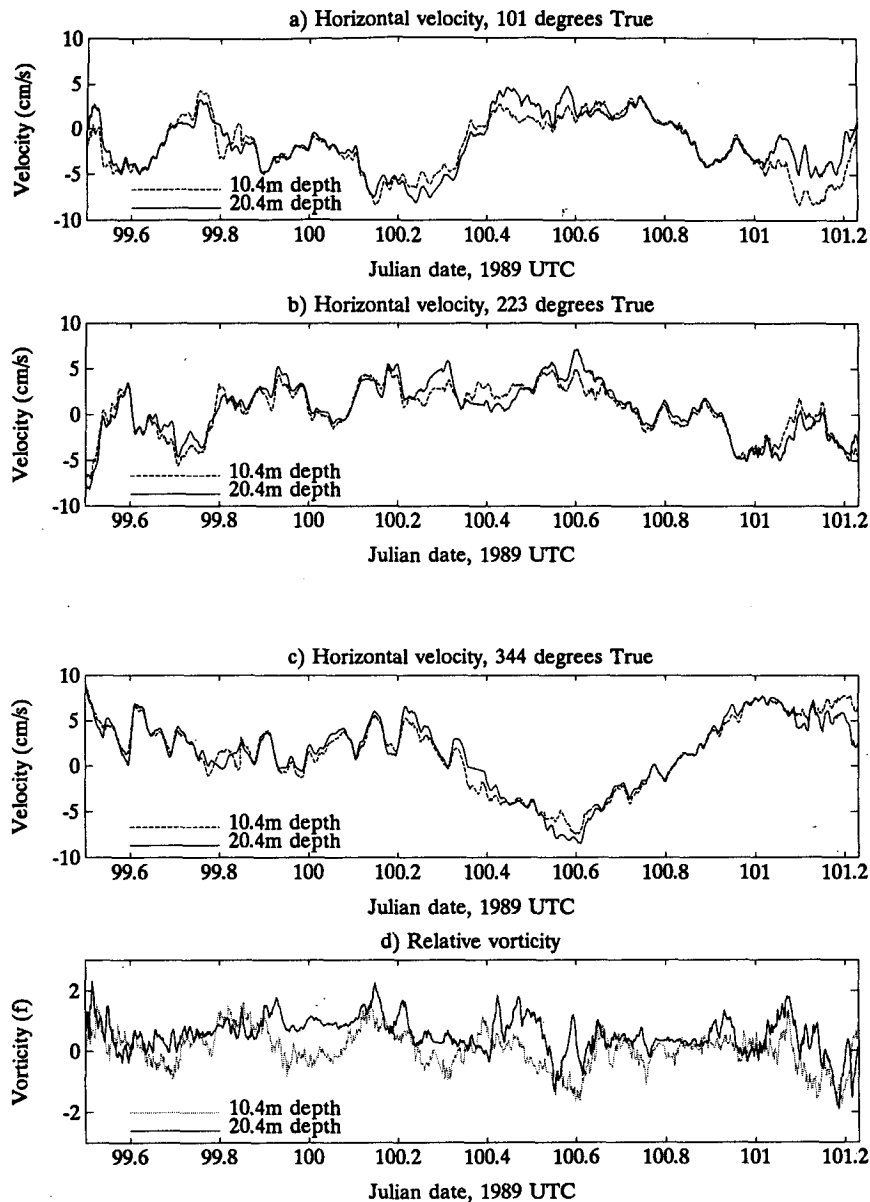


FIG. 16. Comparison of horizontal velocity and vorticity measurements made at depths of 10.4 and 20.4 m. (a) Horizontal velocity, 101°T. (b) Horizontal velocity, 223°T. (c) Horizontal velocity, 344°T. (d) Relative vorticity. (e) Spectra of horizontal velocity, 344°T. (f) Phase of transfer function between 344°T velocity spectra at 10.4 and 20.4 m. (g) Squared coherency of velocity spectra. (h) Spectra of relative vorticity.

3) COMPARISON WITH POINT MEASUREMENTS

McPhee (1992) reports that the significant turbulent eddies for heat and momentum transfer in the boundary layer have typical horizontal extent of order 10–20 m. Therefore, the acoustic current meter averages over several eddies with each sample and attenuates velocity fluctuations due to turbulence. Figure 13 compares path-averaged current measurements with point measurements made by M. G. McPhee (1990, personal communication), using a mechanical current

meter located in the middle of the acoustic array. The solid line represents velocity data from the acoustic path oriented 344°T, low-pass filtered at 0.5 min^{-1} . The dots are 1-min averages from the mechanical current meter. The scatter of the point measurements is a result of the high spatial resolution of the mechanical current meter, which has a sampling wavelength of 20 cm (McPhee 1989), and the turbulent nature of the ice–water boundary layer. The power spectra of the two types of measurements have constant transfer-function phase ($\approx 0^\circ$) and relatively high squared coherency (>0.5) for periods greater than 20 min.

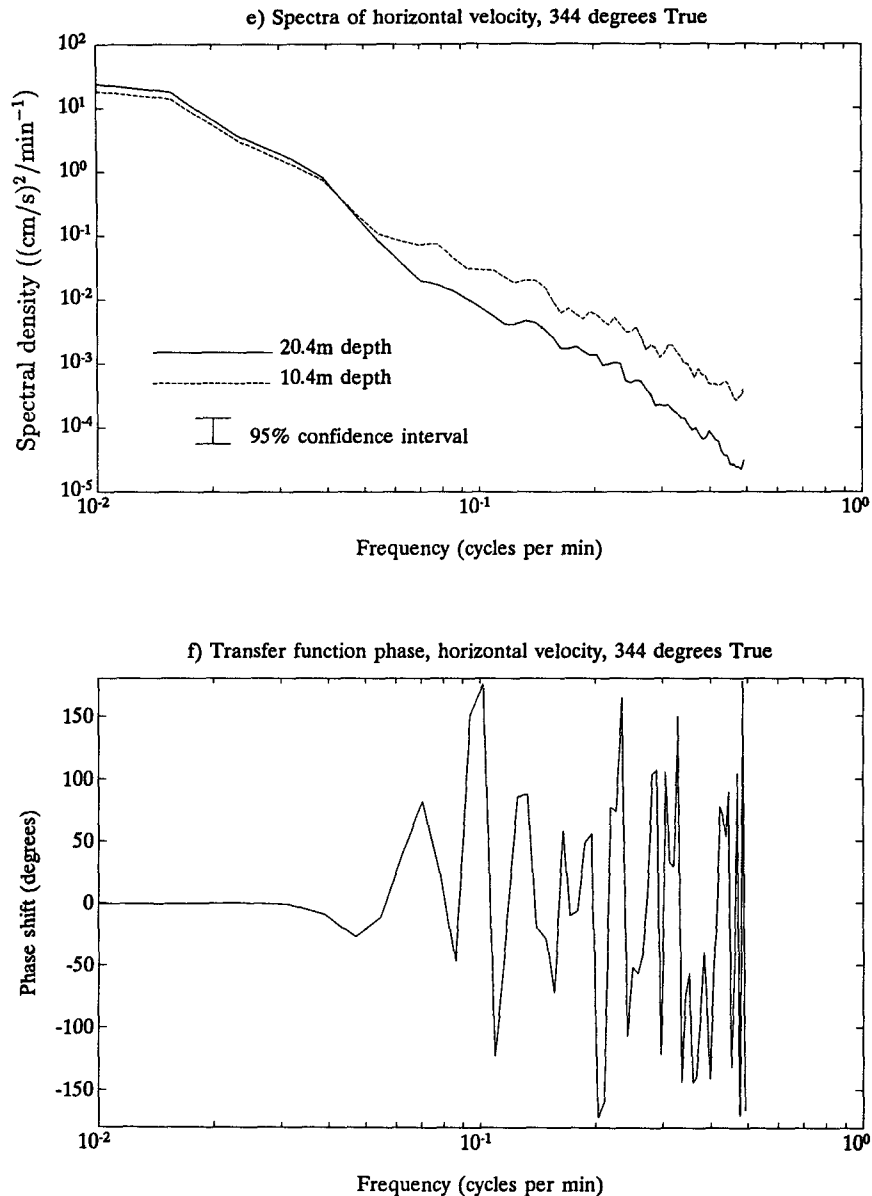


FIG. 16. (Continued)

Each side of the acoustic array preferentially detects internal waves whose wave vectors are aligned with the axis of acoustic propagation. Kinetic energy from internal waves that are not aligned with the acoustic path is attenuated and aliased to lower frequencies. A rough theoretical estimate of the transfer function between point and line-averaged measurements is obtained by assuming that the mean flow is negligible compared to the dispersion velocity of internal waves and that the internal waves propagate parallel to the acoustic path.

The solid line in Fig. 14 is the observed transfer-function magnitude between path-averaged and point measurements. The dotted line represents a theoretical prediction of the transfer function based on the spatial

resolution of the acoustic array given by (26) and a two-layer fluid internal-wave-dispersion relation,

$$\omega^2 = \left(\frac{\rho_2 - \rho_1}{\rho_2 + \rho_1} \right) gk, \quad (27)$$

where $\rho_1 = 1027.47 \text{ kg m}^{-3}$ and $\rho_2 = 1027.87 \text{ kg m}^{-3}$ are the mean water densities above and below the pycnocline as measured during the experiment (Padman and Dillon 1991). Both the measured and the calculated transfer function show strong attenuation for periods shorter than 20 min. The 2-dB difference between the acoustic current measurements and the fixed-point measurements at low frequency results from the less-

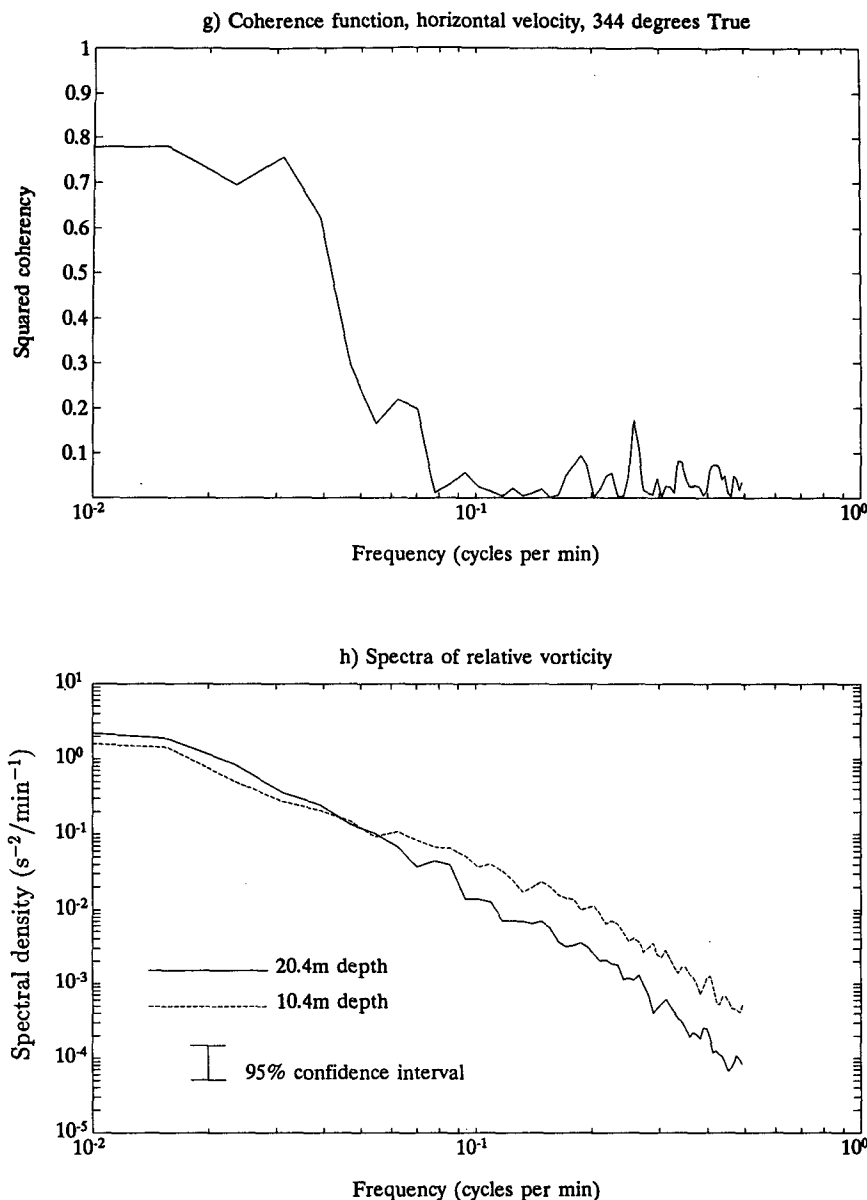


FIG. 16. (Continued)

than-perfect coherence between the two time series. We attribute this discrepancy to local flow anomalies caused by irregularities in the underside of the ice. At high wavenumbers, (26) does not hold, because we cannot assume coherence along the entire acoustic path.

4) DETECTION OF INTERNAL WAVES

Because it attenuates turbulent velocity fluctuations, the acoustic current meter is particularly sensitive to the passage of internal waves that have wavelengths greater than 450 m. Figure 15a shows the signature of a very low-amplitude internal wave train on horizontal current in the mixed layer at 20.4-m depth. This co-

herent wave train was also detected by P. V. Czipott (1990, personal communication) using ice-tilt measurements (Fig. 15b). For small displacements, and neglecting the Doppler shift introduced by ice-camp drift, tilt τ is related to horizontal velocity u_h by

$$\tau = \frac{-1}{g} \frac{\partial u_h}{\partial t} \quad (28)$$

(Czipott et al. 1991). The wave train has a period of about 28 min and rms horizontal velocity of 3.5 mm s^{-1} . Using (28), the expected tilt is $\omega u_h / g = 1.35 \text{ } \mu\text{rad}$ rms as measured.

The less-than-perfect coherence and the phase delay between tilt and acoustic current measurements is due

in part to the 337-m separation between the tiltmeter and the acoustic array. The detection of such events demonstrates the surprising sensitivity of path-averaging current measurements and ice tiltmeters to small internal waves.

Because of its sensitivity, the acoustic current meter is well suited to the study of boundary-layer effects on internal-wave velocity structure, and of coupling between internal waves and turbulence in terms of dissipation of internal-wave energy. Neglecting the effects of ice friction and planetary rotation, the expected horizontal velocity of internal waves in the mixed layer,

$$u_h(z) = u_h(0) \cosh(k_h z), \quad (29)$$

is a function of depth z and horizontal wavenumber k_h (Roberts 1975). For example, given a 600-m wavelength, we expect 1.64% attenuation of horizontal velocity at the 10-m depth compared to the 20-m depth. Any additional attenuation may indicate dissipation of internal-wave energy due to frictional effects.

In Fig. 16, we compare internal-wave velocities measured by the acoustic current meter at depths of 10.4 and 20.4 m. For periods greater than 20 min, there is zero lag and good coherence between the measurements at the two depths as shown on Figs. 16f and 16g, respectively. This is consistent with the notion that velocity fluctuations with periods greater than 20 min are principally caused by internal waves that are coherent throughout the boundary layer, while fluctuations with periods shorter than 20 min result mostly from turbulent eddies that have limited vertical extent. The horizontal velocity energy spectra (Fig. 16e) indicate possible attenuation of internal-wave energy and intensification of turbulent kinetic energy as the ice is approached.

e. Vorticity

The vertical component of relative vorticity at internal-wave length scales is difficult to measure with conventional instrumentation, and we are not aware of other successful attempts to measure this parameter in the boundary layer beneath ice. As discussed earlier, the average vorticity inside the triangle spanned by the acoustic array is readily obtained from reciprocal travel-time measurements. Based on the accuracy of current measurements, the rms noise of the vorticity signal averaged over one minute is less than 1% of the planetary vorticity.

M. D. Levine (1989, personal communication) suggested that the passage of internal waves under the ice camp may have a measurable relative vorticity signature due to conservation of potential vorticity as the mixed-layer depth contracts and expands. Provided that there is no input of vorticity, such as might come from frictional effects with the ice, we have

$$\frac{d}{dt} \left(\frac{\zeta + f}{D} \right) = 0, \quad (30)$$

where ζ is the relative vorticity, f the planetary vorticity, and D the depth of the mixed layer.

We test this hypothesis during the passage of an energetic wave packet that propagated under the ice camp between 0000 and 0200 UTC 18 April 1989 (Julian day 108). The internal wave packet propagated in a direction within 20° of true north, that is, almost parallel to the 344°T acoustic path. The waves in the packet had dispersion velocity 45 cm s^{-1} , wavelength 632 m, and period 24 min (Czipott et al. 1991). The size of the acoustic array (approximately one third of the wavelength) is ideally suited to detect vorticity at these scales. The undisturbed depth of the mixed layer before the passage of the packet was 115 m, and the packet causes a maximum excursion of 36 m in the pycnocline. Based on (30), and assuming negligible relative vorticity before the passage of the wave, we expect a vorticity excursion of order $0.3f$.

In Fig. 17 we plot the horizontal velocity parallel to the propagation direction and the relative vorticity at 8.4-m depth during the passage of the wave packet. The measured vorticity is much greater than what can be accounted for by conservation of potential vorticity. In addition, the frequency of the vorticity signal is double that of the internal waves, that is, the interaction of the waves and the ice is nonlinear. We conclude that friction between the boundary layer and the ice is a more important source of relative vorticity than changes in the depth of the mixed layer.

In Fig. 16d we compare relative vorticity measured at two depths. There is very little coherence between the two time series even at periods associated with internal waves. As for velocity spectra (Fig. 16e), the spectra of vorticity (Fig. 16h) indicate low-frequency attenuation and high-frequency intensification as the ice is approached. We found little coherence between horizontal velocity and relative vorticity measurements; therefore, we discount the possibility that the similar behavior of the spectra results from common measurement errors.

5. Summary and concluding remarks

We have measured horizontal currents in the ice-water boundary layer using two path-averaging acoustical methods: scintillation drift and reciprocal transmission. The two methods provide orthogonal components of velocity for each set of acoustic paths. A limitation of our signal-recording scheme restricts the accuracy of the scintillation measurements; the length of the guard sequences used was limited by real-time decoding requirements, and either the direct or the reflected path arrivals were recorded for each transmission because of limited recording bandwidth. The present measurements, however, demonstrate that the use of the full signal and appropriate analysis would allow excellent scintillation flow measurements.

Reciprocal-transmission measurements are contaminated by relative motion of the acoustic elements

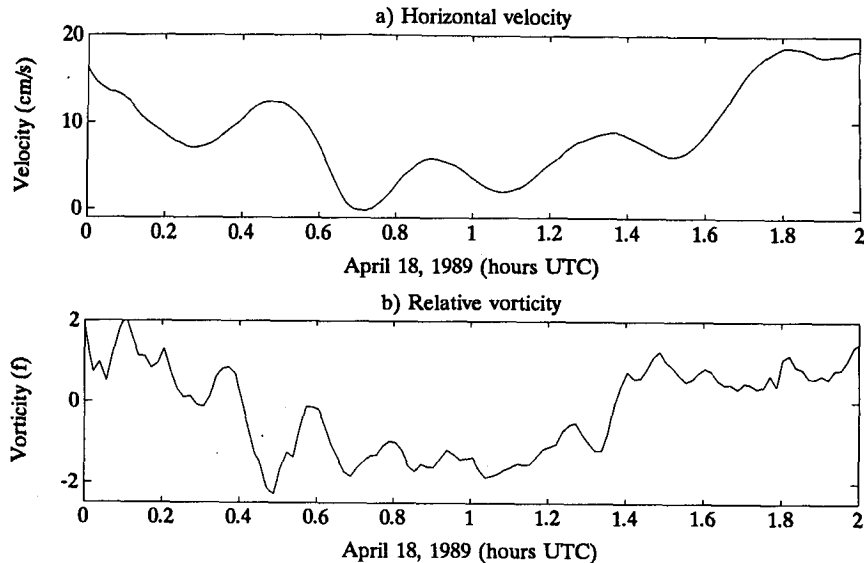


FIG. 17: Vorticity at the 8.4-m depth forced by the passage of an energetic internal-wave packet under the ice camp. (a) Horizontal velocity, 344°T. (b) Relative vorticity.

during each reciprocal transmission for frequencies in the neighborhood of the mooring's mechanical resonance. At frequencies away from this resonance, the noise floor results from interference of the ice-reflected acoustic path with line-of-sight propagation that, as pointed out earlier, could have been overcome with full signal recording or the use of longer guard sequences for decoding. Nevertheless, the rms noise level for the actual horizontal velocity measurements using reciprocal transmission is less than 0.1 mm s^{-1} averaged over 1 min.

Comparison of path-averaged velocity to point measurements shows marked differences that we attribute to local anomalies of the flow field caused by the rough ice topography. The acoustic system provides integral measurements that average over several turbulent eddies; therefore, the measured horizontal velocity is particularly sensitive to the passage of low-amplitude internal waves under the ice camp. A comparison of horizontal velocity at two depths in the boundary layer shows good coherence at internal-wave frequencies and some attenuation as the ice is approached.

Relative vorticity averaged over the span of the acoustic array was measured to an accuracy of $0.01 f$ for a filtered sampling rate of 1 min. Vorticity at internal-wave length scales is dominated by horizontal shear caused by interaction with ice topography and not by planetary vorticity as we initially expected.

In theory, scintillation drift around the triangular array can be used to obtain horizontal divergence. We were unable to obtain meaningful measurements of horizontal divergence during the experiment because of insufficient signal to noise ratio. This was due to a processing and recording design limitation rather than to any inherent limitation of the scintillation approach.

The sensitivity of the instrument allows detection of kinetic energy at frequencies associated with the advection and evolution of turbulent velocity fine structure. Acoustic amplitude scintillation provides information about refractive-index variability along the acoustic path. Therefore, the combination of the two measurements should provide a way to separate the effects of velocity fine structure on acoustic propagation from the effects of sound-speed structure. This, however, remains a goal for future work.

Acknowledgments. We thank Paul Krauetner, P. C. Balla, Ron Teichrob, and Jasco Research for developing the electronics; Syd Moorhouse and Oceanetic Measurements for designing the moorings; Ron Teichrob, Mike Welch, Pat McKeown, and Tom Lehman for help during deployment and recovery; Peter Czippott, Miles McPhee, Murray Levine, and Robin Williams for helpful discussions and making their data available. We are grateful to Schlomo Pauker and two anonymous reviewers for their very constructive criticism of the original manuscript. This work was supported by U.S. Office of Naval Research Grant N00014-88-J-1102, and the first author was funded by scholarships from the Natural Sciences and Engineering Research Council and the Science Council of British Columbia.

APPENDIX A

Correlation Peak Interpolation

In this appendix, two methods for interpolating the location t_0 and amplitude A of correlation peaks are presented. In the first method, a theoretical expression for the shape of the peak is derived and a nonlinear curve-fitting algorithm is applied. The second method

is less accurate, but also easier to implement; a linear least-squares algorithm is used to fit the data to a quadratic.

For the first method, (6), (7), and (8) are used to obtain an expression for the shape of the peak. Since convolution in the time domain becomes multiplication in the frequency domain, (6) can be written

$$\mathcal{R}_{yx}(f) = \mathcal{H}(f) \mathcal{R}_{xx}(f), \quad (\text{A1})$$

where $\mathcal{R}(f)$ and $\mathcal{H}(f)$ are the Fourier transforms of $R(\tau)$ and $h(\tau)$, respectively. The transform of (8) is

$$\mathcal{R}_{xx}(f) = \frac{A \sin^2(\pi f \tau_p)}{\tau_p (\pi f)^2}. \quad (\text{A2})$$

Equations (7), (A1), and (A2) yield the cross correlation as a function of frequency:

$$\mathcal{R}_{yx}(f) = \begin{cases} \mathcal{R}_{xx}(f), & \text{if } -\tau_p^{-1} \leq f \leq \tau_p^{-1} \\ 0, & \text{otherwise.} \end{cases} \quad (\text{A3})$$

The definition of the inverse Fourier transform,

$$R_{yx}(\tau) = \int_{-\infty}^{\infty} \mathcal{R}_{yx}(f) \exp(i2\pi f \tau) df, \quad (\text{A4})$$

standard integral tables, and trigonometric identities are used to solve for $R_{yx}(\tau)$ explicitly:

$$R_{yx}(\tau) = \frac{A}{\pi} \sum_{n=0}^{\infty} \frac{(-1)^n (2\pi)^{2n+1}}{(2n+1)^2 (2n)!} \left[\left(\frac{\tau}{\tau_p} + 1 \right)^{2n+2} + \left(\frac{\tau}{\tau_p} - 1 \right)^{2n+2} - 2 \left(\frac{\tau}{\tau_p} \right)^{2n+2} \right]. \quad (\text{A5})$$

The binomial theorem is applied to convert this expression into a polynomial in even powers of τ/τ_p ,

$$R_{yx}(\tau) = A \sum_{n=0}^{\infty} a_n \left(\frac{\tau}{\tau_p} \right)^{2n}, \quad (\text{A6})$$

with coefficients

$$a_n = \frac{2}{\pi} \sum_{m=n}^{\infty} \frac{(-1)^m (2\pi)^{2m+1} (2m+2)}{(2m+1)(2n)!(2m+2-2n)!}. \quad (\text{A7})$$

Table (A1) gives numerical values for the first ten coefficients. The series in (A6) converges rapidly for $\tau/\tau_p \leq 1$, because successive terms have alternating signs; the maximum error, when n terms are used, is bounded by $A|a_n|(\tau/\tau_p)^{2n}$.

Given data points Y_i corresponding to times t_i , the maximum-likelihood estimate of t_0 and A is obtained by minimizing the merit function

$$\chi^2 = \sum_{i=1}^N [Y_i - R_{yx}(t_i, t_0, A)]^2, \quad (\text{A8})$$

where the correlation delay $\tau = t_i - t_0$. This χ^2 function is minimized using the Broyden-Fletcher-Goldfarb-Shanno algorithm to implement the variable metric method (Press et al. 1986).

TABLE A1. Coefficients of the polynomial that describes the shape of the correlation peak.

n	a_n
0	0.9028233336
1	-2.0000000000
2	1.8599120891
3	-0.9877523383
4	0.3428553005
5	-0.0841722149
6	0.0154094590
7	-0.0021857624
8	0.0002473421
9	-0.0000228505

A second method for interpolating peak location and amplitude is to assume that the peak has a quadratic shape near the maximum and to fit the five recorded data points using linear least squares. For convenience, (10) is expressed in terms of a nondimensional time variable u ,

$$R_{yx}(u) = a + bu + cu^2, \quad (\text{A9})$$

where $u = (t - t_3)/\tau_s$, t_3 corresponds to the central data point, $\tau_s = \tau_p/4$ is the sampling period, and $u_i = i - 3$. The amplitude of the quadratic peak,

$$A_q = \frac{c - b^2}{4a}, \quad (\text{A10})$$

and its location

$$t_0 = t_3 - \frac{b}{2a} \tau_s, \quad (\text{A11})$$

can be expressed in terms of the coefficients of (A9). The merit function that must be minimized is

$$\chi^2 = \sum_{i=1}^5 [Y_i - (a + bu_i + cu_i^2)]^2. \quad (\text{A12})$$

The solution is obtained by use of the normal equations (Press et al. 1986):

$$\begin{bmatrix} a \\ b \\ c \end{bmatrix} = (\mathbf{A}^T \mathbf{A})^{-1} \mathbf{A}^T \begin{bmatrix} Y_1 \\ Y_2 \\ Y_3 \\ Y_4 \\ Y_5 \end{bmatrix}, \quad \mathbf{A} = \begin{bmatrix} 1 & -2 & 4 \\ 1 & -1 & 1 \\ 1 & 0 & 0 \\ 1 & 1 & 1 \\ 1 & 2 & 4 \end{bmatrix}, \quad (\text{A13})$$

where

$$(\mathbf{A}^T \mathbf{A})^{-1} \mathbf{A}^T = \begin{bmatrix} -0.0857 & 0.3429 \\ -0.2000 & -0.1000 \\ 0.1429 & -0.0714 \\ 0.4857 & 0.3429 & -0.0857 \\ 0.0000 & 0.1000 & 0.2000 \\ -0.1429 & -0.0714 & 0.1429 \end{bmatrix}. \quad (\text{A14})$$

APPENDIX B

Shear Effects on Sound Rays

In the presence of shear, the acoustic propagation paths of sound rays traveling in opposite directions between two points do not overlap. This lack of reciprocity may result in an erroneous estimate of path-averaged velocity. In order to estimate the magnitude of this error, we consider changes in acoustic travel time and separation between sound rays traveling in opposite directions.

Consider vertical shear σ such that the horizontal fluid velocity along an arbitrary x axis is

$$u(z) = u_0 + \sigma z. \quad (\text{B1})$$

Without loss of generality, we let $u_0 = 0$ and position two acoustic elements at $x = 0$ and $x = l$ on the horizontal plane $z = 0$ (Fig. B1). Acoustic rays, propagating from $x = 0$ to $x = l$, bend downward if $\sigma > 0$ and upward if $\sigma < 0$.

In a time-independent medium, the acoustic frequency $\omega = 2\pi f$ remains constant along each ray:

$$\omega = k_0(c_0 + u_0 \cos \chi_0) = k[c(z) + u(z) \cos \chi], \quad (\text{B2})$$

where $k = 2\pi/\lambda$ is the wavenumber, $c(z)$ is the vertical sound-speed profile, χ is the grazing angle that the ray forms with a horizontal plane, and $u(z) \cos \chi$ is the component of flow velocity parallel to the acoustic propagation path. By continuity, the horizontal component of the wavenumber vector must also remain constant:

$$k_0 \cos \chi_0 = k \cos \chi. \quad (\text{B3})$$

Eliminating k between (B2) and (B3), we obtain

$$\frac{\cos \chi}{\cos \chi_0} = \frac{c(z) + u(z) \cos \chi}{c_0 + u_0 \cos \chi_0}, \quad (\text{B4})$$

which is Snell's law of refraction, modified by the presence of shear.

If the sound-speed profile is constant, $c(z) = c_0$, then the shear will affect the total travel time $\sum t$, but not the travel-time difference Δt of two acoustic signals propagating in opposite directions. The change in total travel time due to the presence of shear and the maximum separation between opposite sound rays are determined using (B1) and (B4).

In order for sound rays to intersect the x axis at $x = l$, they must leave $x = 0$ with a grazing angle of χ_0 . The turning depth, $\chi = 0$, occurs at the point of maximum separation from the x axis, $z = \eta/2$ and $x = l/2$. The horizontal distance to the turning depth is

$$\frac{l}{2} = \int_0^{l/2} dr = \int_0^{\eta/2} \frac{dz}{\tan \chi}. \quad (\text{B5})$$

We assume $\sigma l \ll 2c$ to solve for range,

$$l = \frac{2c_0}{\sigma} \ln(\sec \chi_0 + \tan \chi_0) \approx \frac{2c_0 \chi_0}{\sigma}, \quad (\text{B6})$$

and initial grazing angle,

$$\chi_0 \approx \frac{\sigma l}{2c_0}. \quad (\text{B7})$$

Referring to Fig. B1, we note that an element of length ds along the propagation path is equal to $dz/\sin \chi$. Therefore, the travel time to $z = \eta/2$ is

$$\frac{\sum t}{4} = \int_0^{\eta/2} \frac{dz}{[c_0 + u(z) \cos \chi] \sin \chi}. \quad (\text{B8})$$

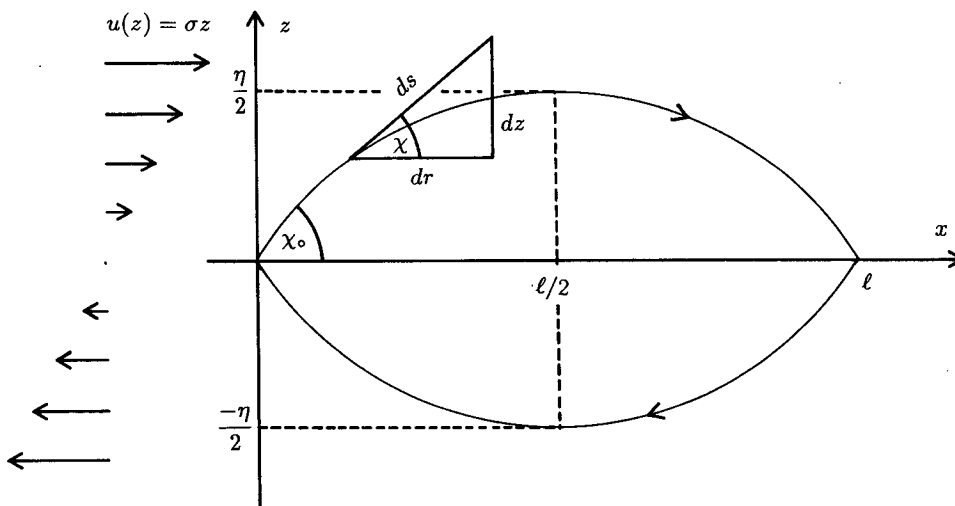


FIG. B1. Ray bending in shear flow. In the presence of shear, sound rays propagating in opposite directions between two points do not follow overlapping trajectories. This may introduce an error in current measurements that rely on reciprocal travel-time difference. This figure defines the variables used to obtain approximate expressions for change in acoustic travel time and maximum separation between opposite sound rays.

We solve for total travel time,

$$\sum t = \frac{2}{\sigma} \tan \chi_0 + \frac{l}{c_0} \cos \chi_0 \approx \frac{2l}{c_0} - \frac{\sigma^2 l^3}{24 c_0^3}, \quad (\text{B9})$$

and note that vertical shear σ decreases the total travel time by approximately $\sigma^2 l^3 / 24 c_0^3$. Finally, we obtain an expression for the maximum separation between sound rays propagating in opposite directions:

$$\eta = \frac{2c_0}{\sigma} (\sec \chi_0 - 1) \approx \frac{\sigma l^2}{4 c_0}. \quad (\text{B10})$$

REFERENCES

- Alonso, M., and E. J. Finn, 1967: *Fundamental University Physics: Mechanics*. Addison-Wesley, 435 pp.
- Carlson, A. B., 1986: *Communication Systems: An Introduction to Signals and Noise in Electrical Communications*. McGraw-Hill, 686 pp.
- Czipott, P. V., M. D. Levine, C. A. Paulson, D. Menemenlis, D. M. Farmer, and R. G. Williams, 1991: Ice flexure forced by internal wave packets in the Arctic Ocean. *Science*, **254**, 832–835.
- Dixon, R. C., 1984: *Spread Spectrum Systems*. Wiley & Sons, 422 pp.
- Farmer, D. M., S. F. Clifford, and J. A. Verrall, 1987: Scintillation structure of a turbulent tidal flow. *J. Geophys. Res.*, **92**, 5369–5382.
- Gupta, S. C., and J. H. Painter, 1966: Correlation analyses of linearly processed pseudo-random sequences. *IEEE Trans. Commun. Technol.*, **14**, 796–801.
- Ko, D. S., H. A. DeFerrari, and P. Malanotte-Rizzoli, 1989: Acoustic tomography in the Florida strait: Temperature, current, and vorticity measurements. *J. Geophys. Res.*, **94**, 6197–6211.
- Longuet-Higgins, M., 1982: On triangular tomography. *Dyn. Atmos. Oceans*, **7**, 33–46.
- McPhee, M. G., 1989: A rigid, cable-lowered instrument frame for measuring turbulence and internal waves in the Arctic. *IEEE J. Oceanic Eng.*, **14**, 203–207.
- , 1992: Turbulent heat flux in the upper ocean under sea ice. *J. Geophys. Res.*, **97**, 5365–5379.
- Morison, J. H., 1989: Physical oceanography instrumentation for the polar regions: A review. *IEEE J. Oceanic Eng.*, **14**, 173–185.
- Müller, P., G. Holloway, F. Henyey, and N. Pomphrey, 1986: Non-linear interactions among internal gravity waves. *Rev. Geophys.*, **24**, 493–536.
- , L. Ren-Chieh, and R. Williams, 1988: Estimates of potential vorticity at small scales in the ocean. *J. Phys. Oceanogr.*, **18**, 401–416.
- Padman, L., and T. M. Dillon, 1991: Turbulent mixing near the Yermak Plateau during the coordinated eastern Arctic experiment. *J. Geophys. Res.*, **96**, 4769–4782.
- Press, W. H., B. P. Flannery, S. A. Teukolsky, and W. T. Vetterling, 1986: *Numerical Recipes*. Cambridge University Press, 818 pp.
- Roberts, J., 1975: Internal gravity waves. *Marine Science*, Vol. 2, Marcel Dekker.
- Rossby, T., 1975: An oceanic vorticity meter. *J. Mar. Res.*, **33**, 213–222.
- Shirasawa, K., 1986: Water stress and ocean current measurements under first-year sea ice in the Canadian Arctic. *J. Geophys. Res.*, **91**, 14 305–14 316.
- Winters, K. B., and D. Rouseff, 1990: A filtered backprojection method for the tomographic reconstruction of fluid vorticity. *Inverse Problems*, **6**, L33–L38.
- Worcester, P. F., 1977: Reciprocal acoustic transmission in a mid-ocean environment. *J. Acoust. Soc. Am.*, **62**, 895–905.
- , R. C. Spindel, and B. M. Howe, 1985: Reciprocal acoustic transmissions: Instrumentation for mesoscale monitoring of ocean currents. *IEEE J. Oceanic Eng.*, **10**, 123–136.